

# Kinematics from spectral lines for AGN outflows based on time-independent radiation-driven wind theory

José M Ramírez

*Leibniz-Institut für Astrophysik Potsdam, An der Sternwarte 16, 14482 Potsdam, Germany*

jramirez@aip.de

## ABSTRACT

We build a bulk velocity-dependent photoionization model of the warm absorber of the Seyfert 1 galaxy NGC 3783. By adopting functional forms for velocity of the flow and its particle density with radius, appropriate for radiation driven winds, we compute the ionization, temperature, line Doppler shift, and line optical depths as a function of distance. By doing this we obtain detailed profiles for the entire absorption line spectrum. The model reproduces the observed relationship between the gas ionization and the velocity shift of the line centroids as well as the asymmetry of the absorption lines in the X-ray spectrum of NGC 3783. It is found that the distribution of asymmetry requires the presence of two outflows: a higher ionization component responsible for the blue wings of the high ionization lines and the red wings of the low ionization oxygen lines, and a lower ionization flow that makes up for the blue wings of the oxygen lines. Our model predicts a relationship between the X-rays and the UV absorbers, where the component creating the long wavelength lines in the X-ray spectrum is also responsible for creating at least part of the UV absorption troughs.

*Subject headings:* AGNs – Photoionization – Plasma – Asymmetry – Absorption lines

## 1. Introduction

X-ray (0.5–10 keV) *Chandra* spectra of type-I active galactic nuclei (AGN) often show presence of absorption lines coming from H- and He-like ions of O, Ne, Mg, Si, S as well as from Fe XVII-Fe XXIII L-shell transitions. These lines are near the region of the bound-free absorption edges of O VII and O VIII at  $\sim 0.8$  keV, which are the hallmark of warm absorbers (George et al. 1998; Komossa 1999). In Seyfert 1 galaxies these absorption lines

can be narrow (Seyfert 1 NALs) with full width at half maximum (FWHM) spanning  $\sim 100$ – $500 \text{ km s}^{-1}$  (Kaspi et al. 2000), or broad (Seyfert 1 BALs) with FWHM  $\sim 500$ – $2000 \text{ km s}^{-1}$  (Kaspi et al. 2001). The troughs of the lines are blue-shifted relative to rest frame of the host galaxy by velocities that go from several hundred to a few thousand  $\text{km s}^{-1}$  (Yaqoob et al. 2003), implying the presence of outflows that cover a wide range of velocities and ionization stages (Kaastra et al. 2000; Kaspi et al. 2002; Krolik & Kriss 2001; Róžańska et al. 2006).

In Seyfert galaxies and Quasars absorption spectra show a range of ionization stages that arise from ionization parameters that span  $\xi \sim 10 - 1000 \text{ erg cm s}^{-1}$  (Kaspi et al. 2002). Simultaneous UV and X-ray observations may enhance this range even further (Shields & Hamann 1997; Gabel et al. 2005). The location of these absorbing material is uncertain. Models of X-ray absorbers in AGN place them in a wide range of distances from the central source, from winds originated at the accretion disk (Murray et al. 1995; Elvis 2000), out to the dusty ( $\sim 1 \text{ pc}$ ) torus (Krolik & Kriss 2001) and beyond the narrow-line region (e.g. Ogle et al. 2000).

In the Seyfert galaxy NGC 3783 the 900 ks *Chandra* spectrum of Kaspi et al. (2002) allows for precise measurements of radial velocities and widths of the lines. It is seen that the velocity shift of lines from Fe XXIII-Mg XII cover a range of  $\sim 60 - 600 \text{ km s}^{-1}$  while the lowly ionized lines Si XIII-O VII cover velocities  $\sim 500 - 1000 \text{ km s}^{-1}$  (see Figure 6 in Ramirez et al. 2005). The average velocity of the warm absorber outflow of NGC 3783 is around  $\sim 500 \text{ km s}^{-1}$ . The spectrum also reveals that the line profiles are asymmetric (Kaspi et al. 2002), in such a way that approximately 90% of the lines have extended blue wings. Such asymmetries were quantified by Ramirez et al. (2005). In terms of ionization, mostly high ionization species are seen in the short-wavelength portion of the spectrum  $\sim 4 - 12 \text{ Å}$ . Here, resonant lines from Fe XXIII, Fe XXII, Fe XXI, S XVI, S XV, Si XIV, and Mg XII cover ionization parameters  $\xi$  from  $\sim 630$  to  $\sim 150 \text{ ergs cm s}^{-1}$ . The longer wavelength of the spectrum,  $\sim 10 - 20 \text{ Å}$ , is dominated by lower ionization lines from Si XIII, Fe XVIII, Ne X, Mg XI, Fe XVII, Ne IX, O VIII, and O VII that span ionization parameters  $\xi$  from  $\sim 125 \text{ ergs cm s}^{-1}$  down to  $\sim 8 \text{ ergs cm s}^{-1}$ .

Thus, photoionization modeling shows that the observed spectrum is hardly explained by a single ionization parameter. Rather two or three components are needed, and this has been the subject of well-detailed studies (Krongold et al. 2003; Netzer et al. 2003; Krongold et al. 2005). In those works two/three components in pressure equilibrium are enough to account for all the charge states seen in the spectra. When start running those simulations, the ionization parameter is not constant throughout the cloud but it varies in a self consistent way. On the other hand Steenbrugge et al. (2003) used a nearly continuous distribution of ionization parameters that span three orders of magnitude. In reality both approaches do not

need to be necessarily contradictory. We just have to look at the possibility of introducing species between the components proposed by Krongold et al. (2003); Netzer et al. (2003); Krongold et al. (2005); and that immediately lead us to the discussion of whether the material absorbing is clumpy or not. And that is in part the goal of the present work. We present both possibilities, continuous *vs* clumpy flows, with their physical implications along the article.

Although there is no evident correlation between the ionization of the absorption species and the velocity shifts of lines (Kaspi et al. 2002), Ramírez et al. (2005) open the possibility for such relationship to exist, as the lines are consistent with being originated from an outward flowing wind. In that work a wind velocity law was adopted (Castor et al. 1975), with an ionization fraction that goes as a power-law of the ionization parameter  $q \sim \xi^\eta$  with  $\eta > 0$  for all  $\xi$  and all lines. Further,  $q \sim \xi^\eta$  and an optical depth of the form proposed by the SEI method from Lamers et al. (1987) were used to fit the line in the spectrum and study the possible relationship between the profiles and the expansion velocity of the flow.

Here, in this theoretical approach no analytical dependence of  $q$  with  $\xi$  is assumed, but computed self-consistently using the photoionization code XSTAR with modifications of the optical depth of the lines for working with expanding outflow.

It is the aim of the present paper to further study the wind scenario for the warm absorber of NGC 3783 by modeling a photoionized wind flow and trying to reproduce the main features in the spectrum in terms of both equivalent widths and line profiles. The model consists of a spherically symmetric gas flow with increasing velocity with radius according to the wind velocity law of Castor et al. (1975). The microphysics of the plasma is then solved in detail along the wind, and radiative transfer is treated for the flowing plasma including Doppler shift effects on the emerging spectrum. This kind of approach has been used previously in studies of the ionization and thermal properties of O stars by Drew (1989), cataclysmic variables by Drew & Verbunt (1985) and in an evaluation of absorption line profiles from winds in AGN by Drew & Giddings (1982).

Self-consistent hydrodynamic modeling of AGNs have been performed in the past (see e.g. Murray et al. 1995) which qualitatively predict the same  $\beta$ -velocity law, where  $v(r) \sim (1 - r_0/r)^\beta$ , as adopted here. However, these models did not include detailed treatment of thermal and spectral processes that lead to synthetic spectra.

The present paper is organized as follows: In §2 we discuss the statistical significance of the X-ray lines under study. Later in §3, we present the theoretical method we have used in this work. In §5 we present the main results of our work. We present the final physical solution in §6. And we summarize in §7.

## 2. Significance of the shifting in the X-ray Lines

Since our analysis searches for possible correlation between ionization state of the ions forming the absorption lines observed in the X-ray spectrum of this object, and the Doppler velocity shift of those lines, we first of all study the statistical significance of this possible shifting. A convenient way to do that is through the separation of the ions into groups and look for the velocity shifting. We take all the ions we find in Table 3. The line’s centroid are taken from Kaspi et al. (2002). The ionization fraction curves for the classification are taken from Kallman & Bautista (2001); Bautista & Kallman (2001). Afterwards we grouping them into three groups <sup>1</sup>: Group (1), representative of all ions of low ionization with ionization parameter  $0 < \xi(\text{ergs cm s}^{-1}) < 10$ ; Group (2)  $10 < \xi(\text{ergs cm s}^{-1}) < 250$  representative of intermediate ionization state; and Group (3)  $250 < \xi(\text{ergs cm s}^{-1}) < 650$ . A graphical way to represent this grouping scheme is with a boxplot shown in Fig 1. Each box is made of five-number summaries: the smallest observation (sample minimum, which are the extreme thin bars at the left of each box), a lower quartile (Q1, which is the left thick border of each box), median (Q2, black thick vertical line), upper quartile (Q3, the right thick border of each box) and largest observation (sample maximum, which are the extreme thin bars at the right of each box). The first conclusion is that all the three Q2s are different. It is clear that Groups 1 and 3 are different at  $\gtrsim 1\sigma$ . There is overlap between Groups 1 and 2 (possible due to limited resolution of the instrument), but Groups 2 and 3 are different at  $\gtrsim 1\sigma$ . We go ahead in our analysis bearing in mind these overlaps in groups.

## 3. Method

Let us consider a radiation source with  $L \sim 10^{44} - 10^{47} \text{ ergs s}^{-1}$ , arising from a super-massive ( $\sim 10^8 M_\odot$ ) black hole (BH). Material  $\sim 0.1\text{--}1 \text{ pc}$  from the BH only needs to absorb a small fraction of this energy to be accelerated to few thousand  $\text{km s}^{-1}$  in Seyfert galaxies and up to  $0.1 - 0.2c$  in high redshift Quasars (Arav et al. 1994; Ramírez 2008; Saez et al. 2009; Chartas et al. 2009). By conservation of mass the number density of hydrogen can be written in spherical symmetry as

$$n_H(r) = \frac{\dot{M}}{4\pi r^2 v(r) \mu m_H}, \quad (1)$$

where  $\dot{M}$  is the mass-loss rate,  $v(r)$  is the outflow speed at radius  $r$ ,  $\mu$  is the mean atomic weight per hydrogen atom and  $m_H$  is the hydrogen mass.

---

<sup>1</sup>We group and generate the figure using the statistical package R - <http://www.r-project.org>

We adopted a velocity law  $v(r)$  compatible with the predictions of the radiatively driven wind theory (Castor et al. 1975). The velocity law has two fundamental roles. The first is to shift the frequency of the absorbing lines according to the Doppler effect. The second is to dilute the gas density, affecting radiative transfer across the gas and consequently the ionization and thermal state of the gas. The velocity law varies with distance as

$$w(x) = w_0 + (1 - w_0) \left(1 - \frac{1}{x}\right)^\beta, \quad (2)$$

here  $w$  is the velocity normalized to the terminal velocity of the wind  $v_\infty$ ,  $w_0$  is the velocity in the base of the wind and  $x$  is the distance normalized to the radius of the central core  $r/r_0$ . The parameter  $\beta$  is the quantity governing the slope of the velocity with the distance and its *ad hoc* value depends on the type of radiative force acting on the wind. Analysis of hot stars suggests that  $0.5 \lesssim \beta \lesssim 1$  (Lamers et al. 1987). The evaluation of radiation-driven wind in AGNs of Drew & Giddings (1982), and more recent dynamical calculations (e.g, Murray et al. 1995; Proga et al. 2000), suggest that in AGNs  $0.5 \lesssim \beta \lesssim 2$ . We have computed models using velocity laws  $\beta = 0.5, 1, 1.5$  and  $2$ , representing from fast ( $\beta = 0.5$ ) to slow winds ( $\beta = 2$ ). We found that fast winds were not able to simultaneously cover the range in velocity and ionization state observed in the spectrum of NGC 3783, needed for the goal of this work, and that the best-fit velocity law was  $\beta = 2$ . This is why for the rest of this work we use  $\beta = 2$ . Then, we rewrite the number density in terms of the velocity law as,

$$n_H(x) = n_0 x^{-2} w^{-1}, \quad (3)$$

where  $n_0 = \left(\frac{\dot{M}}{4\pi\mu m_H} r_0^{-2} v_\infty^{-1}\right)$ . The absorbing line frequencies are shifted according to the Doppler relation,

$$w = \frac{c}{v_\infty} \left(1 - \frac{\lambda}{\lambda_0}\right), \quad (4)$$

where  $\lambda_0$  is rest wavelength.

Our models are based on clouds illuminated by a point-like X-ray source. The input parameters are the source spectrum, the gas composition, the gas density  $n_H(x)$ , and the outflow velocity  $w(x)$ , where  $x$  is the position of each slab inside the cloud normalized to the radius of the most exposed face to the source,  $r_0$ . The source spectrum is described by the spectral luminosity  $L_\epsilon = L f_\epsilon$ , where  $L$  is the integrated luminosity from 1 to 1000 Ryd, and  $\int_1^{1000\text{Ryd}} f_\epsilon d\epsilon = 1$ . This spectral function is taken to be a power law  $f_\epsilon \sim \epsilon^{-\alpha}$ , with  $\alpha = 1$ . The gas consists of the following elements, H, He, C, N, O, Ne, Mg, Si, S, Ar, Ca and Fe. We use solar abundances of Grevesse et al. (1996), in all our models.

Thermal and statistical equilibrium in our models are computed with the code XSTAR (Kallman & Bautista 2001; Bautista & Kallman 2001). The code includes all relevant

atomic processes and computes the equilibrium temperature and optical depths of the most prominent X-ray and UV lines identified in AGN spectra.

We consider two types of models, the single absorber model (SA) and the multicomponent model (MC). In both cases the absorption line profiles depend simultaneously upon the ionization and the kinematics of the absorbing gas.

### 3.1. The Single absorber Model

This model consists of a single extended cloud directly in the line of sight between the observer and the central source. Such a cloud flows away from the central source and towards the observed. For this model we make use of the Sobolev approximation for computing the line optical depths (Castor et al. 1975),

$$\tau_\nu(r) = \frac{\pi e^2}{mc} f \lambda_0 n_i(r) \left( \frac{dv}{dr} \right)^{-1}, \quad (5)$$

where  $f$  is the absorption oscillator strength,  $\lambda_0$  (in cm) is the laboratory wavelength of the transition,  $n_i$  (in  $\text{cm}^{-3}$ ) is the number density of the absorbing ion, and  $dv/dr$  is the velocity gradient in the wind. This gives us the relation between the outflow state and the radiation field. This is different from the calculation of the optical depth in the static case, which is directly proportional to the column density.

Inside the cloud we use a one-step forward differencing formula for the radiation transfer (Kallman & McCray 1982)

$$L_\nu(r + \Delta r) = L_\nu(r) e^{-\tau_\nu(r)} + 4\pi r^2 j_\nu(r) \frac{1 - e^{-\tau_\nu(r)}}{\kappa_\nu(r)}, \quad (6)$$

where  $j_\nu(r)$  is the emission coefficient at radius  $r$ .

Under ionization equilibrium condition the state of the gas depends just upon the shape of the ionizing spectrum and the ionization parameter  $\xi$ , that we define as in Tarter et al. (1969)

$$\xi(r) = \frac{4\pi F(r)}{n_H(r)}, \quad (7)$$

where  $F(r)$  is the total ionizing flux,

$$F(r) = \frac{1}{4\pi r^2} \int_1^{1000\text{Ryd}} L_\nu(r) d\nu, \quad (8)$$

with  $L_\nu(r)$  given by equation (6). The requirement that  $\xi$  spans various orders of magnitude, as observed, yields a cloud geometrically thick throughout most of the spectrum, i.e. a *photoionization bounded* cloud. For instance, a luminosity  $L \sim 10^{44}$  ergs s<sup>-1</sup> and  $\Delta\xi = \xi_2 - \xi_1 = \frac{L}{n}(\frac{1}{r_2^2} - \frac{1}{r_1^2}) = 10^3$  yield  $n \sim 10^6$  cm<sup>-3</sup> and a column density of the absorbing material is  $N_H \sim n\Delta R \sim 9.7 \times 10^{24}$  cm<sup>-2</sup>. This is a large value, such that even lines with moderately small oscillator strengths become saturated in the emergent spectrum, unless the metal abundances are reduced by several orders of magnitude with respect to solar.

In Figure 2 we compare the computed optical depth for the Ne x  $\lambda 12.134$  line in a stationary nebula with  $L = 10^{44}$  ergs s<sup>-1</sup>, and constant density  $n = 10^6$  cm<sup>-3</sup> with a flow with  $n(x) = 3.3 \times 10^6 x^{-0.5} w^{-1}$ , a wind velocity function with  $\beta = 2$ , and  $v_\infty = 1000$  km s<sup>-1</sup>. In both cases we adopt a turbulence velocity of 200 km s<sup>-1</sup> and solar abundances. In the stationary case,  $\tau$  is proportional the column density of the absorbing material and can reach very large values. In the outflow model,  $\tau$  peaks at  $\log \xi \sim 1.3$  ( $v \sim 890$  km s<sup>-1</sup>) reaching  $\sim 5000$ , that is nearly two orders of magnitude smaller than the stationary cloud for the same  $\xi$ . Such high optical depths are common to other lines in the X-ray band, like O VIII in the 14-20 Å and the line O VIII  $\lambda 18.969$ . In such cases lines appear saturated in the absorption spectrum in contrast with observation. In Ramírez et al. (2005) we fit the integrated optical depths of resonant lines in the spectrum of NGC 3783 and found  $T_{tot} \lesssim 1$  for most of the lines. We illustrate in Figure 3 the consequences of taking this model for the reproduction of the profile of the line Ne x  $\lambda 12.134$ . In order to have a non-saturated line (as observed), we had to reduce the abundance to  $\sim 1$  % solar, which has no physical motivation. We do not go further with this model, and present the clumpy (multicomponent) scenario in the next section.

### 3.2. The Multicomponent Model

Now, we examine the scenario in which the absorption profile seen in the X-ray and UV spectra of AGNs are made up of multiple components. The main difference between this model calculations and previous ones by other authors (e.g., Kaspi et al. 2002; Krongold et al. 2003; Róžańska et al. 2006), is that in our model all the components are linked by a velocity law and a gas density distribution.

Each absorber is specified by an ionization parameter  $\xi$ , a column density  $N_H$ , an absorption covering factor, a gas density  $n_H(r)$  and an outflow velocity  $v(r)$  in order to shift the absorption lines according to the Doppler effect. Once the ionic fraction is calculated from the ionization equations, and the ionic levels computed, the opacity in each frequency

bin is

$$\kappa_\nu \rho = \frac{\pi e^2}{m_e c} f_l n_l \left[ 1 - \frac{n_u g_l}{n_l g_u} \right] \phi(\Delta\nu), \quad (9)$$

where  $\kappa_\nu$  is the opacity at the frequency  $\nu$ ,  $\rho = \mu m_H n_H$  is the mass density,  $f_l$  is the absorption oscillator strength,  $n_l$ ,  $n_u$  (in  $\text{cm}^{-3}$ ),  $g_l$ ,  $g_u$  are the number density and the statistical weight of the lower and upper levels of the transition respectively. We allow for the lines to have a finite width characterized by the line profile  $\phi(\Delta\nu)$ , with a width which is the greater between the thermal and the turbulent motions. In all our models the turbulence velocity is assumed to be  $200 \text{ km s}^{-1}$ . The optical depth of a line in each component is

$$\tau_\nu = \int_{r_1}^{r_2} \kappa_\nu(r) \rho(r) dr, \quad (10)$$

where  $r_2$  and  $r_1$  are the limits of the cloud.

It is important to highlight a special difference between the way we use the ionization parameter in the MC model and the way it is used in the SA model. Because of the clouds intervening in this model are optically thin, the ionization parameter at the most exposed face of the cloud remains essentially constant through the cloud, i.e.

$$\xi(r) = \frac{4\pi F(r)}{n_H(r)}, \quad (11)$$

where  $F(r)$  is the total ionizing flux at the radius  $r$ .

When two or more outflows are put together they are assumed to be distributed such that the observed spectrum is the result of the addition of all components. So the radiative flux in each bin of frequency for the composite spectrum is

$$F_\nu = \sum_{i=1}^m f_\nu(x_i) \quad (12)$$

where  $m$  is the number of absorbing clouds in the line-of-sight,  $f_\nu(x_i)$  is the flux resulting from the pass of the continuum radiation through the absorbing cloud “ $i$ ”, and  $x_i$  is the normalized spatial radius of the cloud.

In Ramírez et al. (2005) is showed that in order to fit the line profiles in NGC 3783 a geometry different from the spherical for the gas distribution is required. Such deviation from spherical geometry has two effects. In the normalized notation the number density is

$$n_H(x) = n_0 x^{-2+\kappa} w^{-1}, \quad (13)$$

where  $0 \leq \kappa \leq 2$ . A positive value of  $\kappa$  implies that the gas flow dilutes more slowly than in a free spherical expansion, i.e. that there are sources of gas embedded in the flow, or that



the flow is confined. A negative value corresponds to sinks of gas in the flow, or expansion of an initially confined flow in a flaring geometry. Secondly, we allow the radiation flux to have a form

$$F = F_0 \times x^{-2-p}, \quad (14)$$

where  $p$  is an index to mimic a deviation of flux from the pure geometrical dilution case.

This is expected if the medium between clouds has a significant optical depth (if  $p$  is positive) or if there are sources of radiation embedded in the flow (if  $p$  is negative).

#### 4. Assumption about the number density

Before going into the presentation of the results we would like to highlight important differences between the underlying physical/geometrical motivation of the present work and previous ones. After reviewing single (geometrically thick model) and clumpy (geometrically thin model), we favored the latest one and require for the production of the line profile found in the spectrum of Seyfert galaxies,  $\Delta R/R \ll 1$  (also based on results by Gabel et al. (2005) from UV data).

Based on UV CIII\* density constraints (Gabel et al. 2005), the electron density for the absorber could be  $n_e \approx 10^4 \text{ cm}^{-3}$ . With this (using eq. 11 and  $n_H \approx n_e/1.2$ ), the distance between the absorber and the central source is  $R \approx 25 \text{ pc}$  ( $\approx 10^{20} \text{ cm}$ ). As in Gabel et al. (2005), the low ionization species (XLI in that paper) seems to share the same kinematics with the UV absorber. Using typical luminosity  $L$  for this object of  $\approx 10^{44} \text{ ergs s}^{-1}$ ,  $n_H \approx 10^4 \text{ cm}^{-3}$ , ionization parameter of  $\xi \approx 1$ ,  $R \approx 10^{20} \text{ cm}$ ; similar to that computed by Gabel et al. (2005), but if we take  $n_H \approx 10^{11} \text{ cm}^{-3}$ , as is required for  $\Delta R \ll R$ ; then  $R \approx 10^{16.5} \text{ cm}$ . This is not in contradiction with Krongold et al. (2005), where they set limits on the density and location of the absorber; with  $n_e > 10^4 \text{ cm}^{-3}$ , and  $D < 5.7 \text{ pc}$ . However is clearly different from the computation made by Netzer et al. (2003), of  $n_e < 5 \times 10^4 \text{ cm}^{-3}$   $D > 3.2 \text{ pc}$  for the  $\log(U_{ox}) = -2.4$  component,  $n_e < 10^5 \text{ cm}^{-3}$   $D > 0.63 \text{ pc}$  for the  $\log(U_{ox}) = -1.2$  component, and  $n_e < 2.5 \times 10^5 \text{ cm}^{-3}$   $D > 0.18 \text{ pc}$  for the  $\log(U_{ox}) = -0.6$  component. It is clear that some of the differences in the estimations can be due to differences on the nature of the physics behind the estimations. In Krongold et al. (2005) (and also Reeves et al. (2004) for the Fe K shell), the fundamental assumption behind the computation of  $n_e$  is that the absorber responds instantaneously to changes of flux in the ionizing source, while in Netzer et al. (2003) the estimations are based on temperature derived models, average recombination rates and no response to continuum variations on timescale of 10 days. And, for our purposes, that basically translate in differences between the two proposed physical mechanisms; thermally accelerated winds, which from grounds has to consider sublimation radius for the material

not being evaporated, and radiatively accelerated wind with origin possibly in the accretion disk with subparsec scales; both competitor theories in the explanation of the origin of the warm-absorber outflows.

## 5. Results and Discussions

In Figure 4 we show the variation of the different variables governing the kinematics and the ionization structure of one of our models (model A). This is a wind with a velocity slope  $\beta = 2$ ,  $\kappa = 1.5$  and  $p = 1.5$ . The number of kinematic component  $m$  is 11. The assumed abundance is solar as is given in Table 1, and each component has a column density of  $N_H = 5 \times 10^{20} \text{ cm}^{-2}$ . In this model the variation in the ionization parameter is  $\log \xi = 3.5 - (-0.65)$  [erg cm/s], where the “launching” ionization parameter is defined as  $\log \xi_0 = 3.5$  [erg cm/s], and the variation in density  $\log n_H = 11.4 - 10.26$  [cm $^{-3}$ ]. We can see the variation with distance of the input parameters  $w$ , flux,  $n_H$  and  $\xi$ , for model A in Figure 4. In Figure 5 we plot the velocity shifts taken from the maximum line optical depths  $\tau_{max}$  of our model versus the line centroids measured by Kaspi et al. (2002) for NGC 3783 (see Table 3 in that paper).

We fit a linear model by robust regression using the M estimator (Huber 1964). The weights are included as the inverse of the variances, with the variance equal to  $\Delta v = (v_{lo} + v_{hi})/2$ , and  $v_{lo}$ , and  $v_{hi}$  are the differences between centroid and lower and upper velocity limits of the measured lines given in Table 3 of Kaspi et al. (2002). The best-fit slope is  $0.97 \pm 0.31$  (solid line in the figure), and the residual standard error (rms) is 15.4 for 25 degrees of freedom (dof). This agreement is encouraging considering that no model have been suggested before to explain the possible correlation between the ionization parameter and the velocity shift seen in this Seyfert galaxy.

Although the velocity shifts measured with respect to line minima are well explained by this model the distribution (in general) of line profile shapes is not in agreement with that reported in Ramírez et al. (2005), for instance. From that study most lines have extended blue wings. On the other hand, the model does predict the correct asymmetries for a few lines from highly ionized species, but the profiles of the lower ionizations lines exhibit more extended red wings, unlike observations. The discrepancy between the modeled profile of the O VIII  $\lambda 18.9$  line and the observed in NGC 3783, is important. This is why we created model B.

In Figure 6 we present the variation of the variables governing the kinematics and the ionization structure of another model (model B). Here we change slightly the parameters

$\log \xi_0$ , and  $v_\infty$  (see Table 2 for details). The wind has the parameters  $\beta = 2$ ,  $\kappa = 1.5$  and  $p = 1.5$ . The number of kinematic component  $m$  is 11. The abundances and the column density are as in model A. In this model the variations in ionization parameter and density are  $\log \xi = 3.00 - (-1.13)$  [erg cm/s] and  $\log n_H = 11.40 - 10.26$  [cm<sup>-3</sup>]. We compare models A and B in terms of the variation of optical depth vs. velocity of the flows of three important lines, i.e, Si XIV  $\lambda 6.182$ , Si XIII  $\lambda 6.648$  and Mg XII  $\lambda 7.106$ . We could estimate the contribution of each cloud to the formation of the composed profiles of these lines. We have that model B is superior to model A in describing the low-velocity portion of the flow reflected by the high ionization lines seen in NGC 3783 (extended blue wings), but yields a worse description of the spectrum at higher terminal velocities responsible for the center of the lines measured by Kaspi et al. (2002). Figure 7 shows the fit of a linear model by robust regression using the M estimator for model B. As in model A, the weights are included as the inverse of the variances, with the variance equal to  $\Delta v = (v_{lo} + v_{hi})/2$ , and  $v_{lo}$ , and  $v_{hi}$  are the differences between centroid and lower and upper velocity limits of the measured lines given in Table 3 of Kaspi et al. (2002). The best-fit slope is  $0.72 \pm 0.20$  (solid line in the figure), and the residual standard error (rms) is 17.6 for 25 degrees of freedom (dof). In general, the scatter get worse for lines with terminal velocities greater than 1100 km s<sup>-1</sup>.

### 5.1. Modeling global properties - $\xi$ vs velocity

One of the prime goals of this study is to examine the relationship between the kinematics and the ionization structure of the flow. This is in complement with earlier works (Krongold et al. 2003; Netzer et al. 2003; Krongold et al. 2005) which follow the algorithm of constructing a grid of static photoionization models varying in ionization parameter and column density with the selection of this quantities which best reproduce the EW observed in the spectra, in addition paying attention to the relationship between these physical parameters and the position in wavelength space of the absorption troughs.

Krongold et al. (2003) fitted photoionization models to the 900 ks spectrum of NGC 3783 using two phases; one at high ionization and high temperature  $\log T \sim 5.98$  (HIP) and one at low ionization and temperature  $\log T \sim 4.41$  (LIP), finding good agreement between the modeled equivalent width (EW) and the measured for a set of absorption lines (see Figure 9 of Krongold et al. (2003)). They set each of these phases at a single outflow velocity of  $\sim 750$  km s<sup>-1</sup>, assuming spatial coexistence of the two absorbers. The approach is similar to that from Netzer et al. (2003), but in the latest one they use three components in pressure equilibrium, with two kinematic components each.

One property of our model is the capability of open the possibility of establishing <sup>2</sup> a relationship between the ionization and the kinematics of the gas based on a radiatively accelerated wind. Figures 8 and 9 show this relation for models A and B respectively. In these plots show the predicted relationship between observed velocities and ionization parameter. While absorption from highly ionized ions originates from low-to-intermediate (200-600 km s<sup>-1</sup>) velocities, lines from lower ionization stages are formed at intermediate-to-high velocities (600-1000 km s<sup>-1</sup>).

## 5.2. Far-UV and UV absorbers

The relationship between the X-ray absorption spectrum and the UV absorption spectrum is at present a subject of controversy. Kraemer et al. (2001) and Gabel et al. (2003, 2005) have analyzed the UV spectrum of NGC 3783. HST/STIS and FUSE spectra show absorption troughs from the low order Lyman series (i.e. Ly $\alpha$ , Ly $\beta$ , Ly $\gamma$ ), C IV  $\lambda\lambda$ 1548.2, 1550.8, N V  $\lambda\lambda$ 1238.8, 1242.8, O VI  $\lambda\lambda$ 1032, 1038. All these lines are seen in three kinematic components at  $-1365$ ,  $-548$ , and  $-724$  km s<sup>-1</sup> (components 1, 2 and 3 respectively). A weak fourth component is reported by Gabel et al. (2003, 2005) at  $-1027$  km s<sup>-1</sup>. Figure 10 shows the spectrum predicted by model B in the range 700–1700 Å. It is clear from this figure that lines due to low order Lyman series, He II, C IV, N V, O VI, and Ne VIII would be detectable in the UV band of the spectrum. Figure 11 shows the spectra of several UV lines as a function of radial velocity respect to the systemic. At the top of the Figure we present the Ly $\alpha$  blended with the He II  $\lambda$ 1215 line (upper left) which yields a feature centered at  $\sim -1300$  km s<sup>-1</sup>. Also an absorption feature is formed with the Ly $\beta$  and He II  $\lambda$ 1025 lines (upper center) with center at  $\sim -1200$  km s<sup>-1</sup>, and the line Ly $\gamma$  (upper right) with a velocity  $\sim -1100$  km s<sup>-1</sup>. At the bottom of the Figure we plot the spectrum of three important doublets (C IV  $\lambda\lambda$ 1548.2, 1550.8, N V  $\lambda\lambda$ 1238.8, 1242.8, and O VI  $\lambda\lambda$ 1032, 1038). The solid line depicts the velocity spectra constructed taking the shorter wavelength of the doublet. The spectra in dashed lines were made taking the longer wavelength. One can see the similarity between the velocities predicted by our model and the high-velocity components (1, 4 and likely 3) seen in the UV spectrum of NGC 3783 and others Seyfert 1 galaxies (for example NGC 5548). This is similar to the conclusion reached by Gabel et al. (2005), based on Kaspi et al. (2002) and Gabel et al. (2003), where all X-ray lines having sufficiently high-resolution and S/N were found to span the radial velocities of the three UV kinematic components (see also next section). These are predictions which arise naturally

---

<sup>2</sup>We explicitly state *open the possibility*, since the limited resolution of the telescope does not allow us to go beyond this possibility.

from our model because we are modeling the wind self-consistently with complete treatment of radiative processes in all wavelengths. In our models these UV features as well as the long wavelength absorption lines in the X-ray band, are produced by the low ionization parameter part of the flow (e.g.  $\log \xi = 0.12, -1.13$  from Figure 6 lower right panel). This demonstrates that the same absorber can produce X-ray and UV lines with similar velocities. Figure 12 shows the kinematic relationship between the X-ray and the UV absorbers. The model has been shifted (up) for clarity. Here we show the O VIII  $\lambda 18.969$  and the doublet O VI  $\lambda\lambda 1032, 1038$  (with respect to the shorter wavelength). For comparison we plot the histogram data of the 900 ks of NGC 3783. We see that our model is capable of simultaneously producing X-ray and UV absorption lines with similar velocities around  $\sim 1000 \text{ km s}^{-1}$ , as it has been suggested from UV data (Gabel et al. 2003).

### 5.3. Present single wind *vs* Multiphase wind scenario

However, we want to highlight the most important differences between our model, consisting of a single wind, governed by the laws of radiative acceleration and the multiphase wind; subjected to pressure equilibrium.

The first difference is that in our model there is a clear correlation between ionization state of the ions and velocity ( $\xi - v$ ), and  $\xi$  and number of particle  $n_H$  ( $\xi - n_H$ ). At the same time because of the dependence of  $v$  and  $n_H$  on the spatial distance  $r$ , a dependence of  $\xi$  on  $r$ . This is different from the multicomponent in pressure equilibrium model, suggested by Netzer et al. (2003). In that model three components (in ionization) may coexist in the same volume of space, and lying on the stable regions of the nearly vertical part of the thermal stability curve ( $\log T$  *vs*  $\log[U/T]$  see Figure 12 in that paper). Our absorbers are not embedded in an external medium, and they cannot coexist at exactly the same location but follow the physical laws of radiative acceleration. In that context, Gabel et al. (2005) also find that the UV absorbers of NGC 3783, may share some properties of the multiphase thermal wind. The UV kinematic components 1b, 2 and 3 could occupy the low-temperature base of the region of the thermal stability curve where a range of temperatures can coexist at pressure equilibrium. There is one weak point in the picture of inhomogeneities coexisting at pressure equilibrium. The low-ionization high-velocity UV absorber does not fit there, due to a factor of 10 larger pressure than the other component. If embedded into a more ionized-hotter material, it will eventually evaporate, unless there exist an additional confining mechanism. This extra confining could be provided by magnetic pressure, requiring moderate magnetic fields ( $B \approx 10^{-3} \text{ G}$ ), as is predicted by some dynamical models (Emmering et al. 1992; de Kool & Begelman 1995). In our model, there is no need for confining mechanism, and if

any the more ionized material is closer to the source shielding the intense continuum radiation preventing its evaporation. We conclude by stating that our model is one competitor more, it cannot be ruled out compared with pressure equilibrium model. A more detailed comparison between models is beyond the scope of the present work, that could take place somewhere in the future.

## 6. Two outflows

So far we have been concerned with the line velocity shifts as measured with respect to the points of maximum absorption of the lines, but little have been said about the asymmetry of the troughs. To quantify the line asymmetries predicted by the theoretical models we have tabulated the fraction of the terminal velocity at which the absorption is maximum, to be compared with the ratio  $(\bar{v}/v_1)$ , where  $v_1$  is the position of the blue edge of each line, used to quantify the asymmetry in the spectrum of NGC 3783, see Table 3 of Ramírez et al. (2005). We characterize a theoretical line as “red” if  $v(\tau_{max})/v_\infty > 0.5$  and as “blue” if  $v(\tau_{max})/v_\infty < 0.5$ , while for observed lines they are grouped with respect to  $\bar{v}/v_1 > 0.5$  and  $\bar{v}/v_1 < 0.5$  (see Ramírez et al. 2005). In Table 3 we present the observed troughs. In the first and second columns are the identifications and the wavelengths of the lines, in the third we give the fraction  $v(\tau_{max})/v_\infty$  for model A, and in the fourth column the classification from observed lines, as in Ramírez et al. (2005), i.e.,  $\bar{v}/v_1$ . We classify every trough as either (R) if it is red or (B) if it is blue. There are clear discrepancies between model A and observation. In order to improve on the agreement with observations we found necessary to create a model composed by two outflows, which differ by their  $\log \xi_0$ , the initial exposition to the source. In table 4 we can see the parameters of the two outflows separately, which composed model C. The first flow with  $\log \xi_0 = 3$ , which we call HIF (stand from high ionization flow), is able to create the majority of the high ionization lines (S xvi  $\lambda 4.729$ , S xv  $\lambda 5.039$ , Fe xxiii  $\lambda 8.303$ ), with extended blue wings as the flow moves outwards, and acquires more velocity, in agreement with the observations. The second, which we call LIF (stand from low ionization flow), is characterized by  $\log \xi_0 = 2$ , is able to create the extended blue wing of the oxygen lines. This model has the fundamental ingredients that explain the asymmetry observed in the lines of NGC 3783 and at the same time, gives us the bulk velocity of the flow.

In the third column of Table 5 we present the characterization of the lines coming from the two-outflows model. The HIF component, is the major contributor to the formation of the high ionization lines, i.e. S xvi, Fe xxi, Fe xxii, Fe xxiii, because their optical depths peak close to  $\log \xi_0(\text{HIF})$ , and as the velocity of the flow increases their ionization fraction

decrease, forming their blue wings. Under this picture, only a few lines are characterized as blue, while the rest are red. Some intermediate-to-low ionization ions, have appreciable fractions in the LIF component, which broadens the lines and yields a red apparenity to the composed profile. This effect is illustrated by the fourth column of Table 5.

The composed model reproduces the asymmetry of the lines. The present uncertainties in the computation of  $v(\tau_{max})$  are of the order of  $60 \text{ km s}^{-1}$  (or  $\Delta v(\tau_{max})/v_\infty = 0.055$  with  $v_\infty = 1100 \text{ km s}^{-1}$ ). So the lines classified as pure red with  $v(\tau_{max})/v_\infty \gtrsim 0.55$  and pure blue with  $v(\tau_{max})/v_\infty \lesssim 0.45$  are more reliable than those with  $0.45 \lesssim v(\tau_{max})/v_\infty \lesssim 0.55$ .

It is interesting to analyze why the O VII and O VIII lines are blue, while the lines Mg XI  $\lambda 7.473$  and Fe XVII  $\lambda 15.015$ , remain red. The optical depths of Mg XI  $\lambda 7.473$ , and Fe XVII  $\lambda 15.015$  are below  $10^{-4}$  at velocities greater than  $1100 \text{ km s}^{-1}$ , so the LIF component does not contribute to their broadening. Another interesting example is the difference in classification between the lines Mg XI  $\lambda 7.473$  and Mg XI  $\lambda 9.169$ . The reason is that while for Mg XI  $\lambda 7.473$  the oscillator strength is  $\sim 5 \times 10^{-2}$ , the f-value for the line Mg XI  $\lambda 9.169$  is almost one order of magnitude higher ( $\sim 7 \times 10^{-1}$ ), which makes the optical depth of the latter significant up to velocities beyond  $\sim 1600 \text{ km s}^{-1}$ .

Figure 13 compares the modeled velocities of the lines from the two-outflows model with observations. Robust regression using the M estimator gives a slope of  $0.63 \pm 0.22$  (solid line in the figure), and the residual standard error (rms) is 16.6 for 25 degrees of freedom (dof).

A comparison between the predicted trough profiles and those observed in NGC 3783 is shown in Figure 14. Here we plot the theoretical spectrum given by the outflows HIF and LIF, in the  $18.5 - 19.3 \text{ \AA}$ . Here we have used a powerlaw as continuum with spectral index of  $\Gamma = 1.77$ , suitable for this AGN, set an extra absorber the **wabs**<sup>3</sup> model in XSPEC, and the composed fluxes generated by the HIF and the LIF components. To compose the O VIII  $\lambda 18.969$  line profile we have summed the fluxes from both flows using the equation (12) (where  $m = 22$ ). With this approximation the profile predicted by the two-outflows model is in excellent agreement with the observation Ramírez et al. (2005). The red wing of the troughs, in the range  $0-1000 \text{ km s}^{-1}$ , is formed by the HIF, while the blue wing, in the range  $\sim 1000-2500 \text{ km s}^{-1}$ , is formed by the LIF. These values are in agreement with the values measured for this lines in the observed spectrum.

It is the first time that such theoretical work is performed to explain the asymmetry seen in absorption in the X-ray spectrum of AGNs. Other works have been able to explain the blue wings of UV lines, like the well-studied C IV  $\lambda 1549$ , for example from radiation-

---

<sup>3</sup>N<sub>wabs</sub> =  $0.1 \times 10^{22} \text{ cm}^{-2}$ .

driven disk-wind models (Proga 2003). So we cannot conclude that the model presented here is unique for the description of the asymmetry seen in X-ray lines of AGNs, until detailed comparisons are made with such models, including X-ray line profile produced by a wind from a Keplerian accretion disk (Knigge et al. 1995; Shlosman et al. 1996; Proga et al. 2000; Drew & Proga 2000). Further work is necessary to be performed for such comparison and we plan to do that in a near future.

## 7. Summary

We have computed photoionized wind-flow models for the X-ray spectrum of NGC 3783. We studied singly continuously absorbing models as well as multiple optically thin components linked through an analytic wind velocity law. It is found that the singly continuously absorbing model yields gas column densities and optical depths too high, unless one adopts very low ( $\sim 10^{3-4} \text{ cm}^{-3}$ ) densities and metal abundances ( $\sim 0.01$  solar). On the other hand, the multicomponent model is able to reproduce observations very well. For this model we compute ionization properties of the material using a velocity law compatible with a radiative wind. Our model is consistent with  $\log n_0 \sim 11.35 [\text{cm}^{-3}]$ , a launching radii of  $\log r_0 \sim 15 [\text{cm}]$ , and a terminal velocities of  $v_\infty \sim 1500 \text{ km s}^{-1}$ , which yields a mass loss rate of the order of  $\dot{M}_{out} \sim 1 \text{ M}_\odot/\text{yr}$  (assuming a volumic factor  $f_{vol} = 0.1$ ). If we assume an ionizing luminosity of  $L \sim 2 \times 10^{44} \text{ ergs s}^{-1}$  (Peterson et al. 2004), and accretion efficiency of  $\eta = 0.1$ , the Eddington mass accretion mass is  $\dot{M}_{edd} \sim 0.01 \text{ M}_\odot/\text{yr}$ . This is consistent with the result of Crenshaw & Kraemer (2007) for NGC 4151, and Ramírez (2008) for APM 08279+5255, of  $\dot{M}_{out}/\dot{M}_{edd} > 10$ . However, it is different from the supposition made by Gonçalves et al. (2006), of  $\dot{M}_{out}/\dot{M}_{edd} \leq 1$ , using their photoionization code TITAN, for computing the single medium in pressure equilibrium.

Finally, the asymmetry seen in the lines of the X-ray spectrum of NGC 3783 required a model with two outflows. One flow with a launching ionization parameter of  $\log \xi_0 \sim 3$  and a column density of  $N_H = 10^{22} \text{ cm}^{-2}$ , which recreates the red wings of the low ionization lines from Ne IX to O VII, and the blue wings of the high ionization lines from Fe XXIII to Si XIV. A second flow is necessary to create the blue wing of the oxygen lines, which exhibit a blue character, the theoretical fitting required  $\log \xi_0 \sim 2$ , terminal velocities of around  $\sim 2200 \text{ km s}^{-1}$ , and a column density of  $N_H = 10^{21} \text{ cm}^{-2}$ .

Our calculations also predict a relationship between the UV and X-ray bands, as models adjusted to fit the X-ray spectrum naturally predict UV lines like the Lyman serie, and the O VI, N V and C IV doublets, in apparent concordance with Costantini (2010).



## REFERENCES

- Arav, N., Li, Z., & Begelman, M. C. 1994, *ApJ*, 432, 62
- Bautista, M. A. & Kallman, T. R. 2001, *ApJS*, 134, 139
- Castor, J. I., Abbott, D. C., & Klein, R. I. 1975, *ApJ*, 195, 157
- Chartas, G., Saez, C., Brandt, W. N., Giustini, M., & Garmire, G. P. 2009, *ApJ*, 706, 644
- Costantini, E. 2010, ArXiv e-prints
- Crenshaw, D. M. & Kraemer, S. B. 2007, *ApJ*, 659, 250
- de Kool, M. & Begelman, M. C. 1995, *ApJ*, 455, 448
- Drew, J. & Giddings, J. 1982, *MNRAS*, 201, 27
- Drew, J. & Verbunt, F. 1985, *MNRAS*, 213, 191
- Drew, J. E. 1989, *ApJS*, 71, 267
- Drew, J. E. & Proga, D. 2000, *New Astronomy Reviews*, 44, 21
- Elvis, M. 2000, *ApJ*, 545, 63
- Emmering, R. T., Blandford, R. D., & Shlosman, I. 1992, *ApJ*, 385, 460
- Gabel, J. R., Crenshaw, D. M., Kraemer, S. B., Brandt, W. N., George, I. M., Hamann, F. W., Kaiser, M. E., Kaspi, S., Kriss, G. A., Mathur, S., Mushotzky, R. F., Nandra, K., Netzer, H., Peterson, B. M., Shields, J. C., Turner, T. J., & Zheng, W. 2003, *ApJ*, 583, 178
- Gabel, J. R., Kraemer, S. B., Crenshaw, D. M., George, I. M., Brandt, W. N., Hamann, F. W., Kaiser, M. E., Kaspi, S., Kriss, G. A., Mathur, S., Nandra, K., Netzer, H., Peterson, B. M., Shields, J. C., Turner, T. J., & Zheng, W. 2005, *ApJ*, 631, 741
- George, I. M., Turner, T. J., Netzer, H., Nandra, K., Mushotzky, R. F., & Yaqoob, T. 1998, *ApJS*, 114, 73
- Gonçalves, A. C., Collin, S., Dumont, A., Mouchet, M., Róžańska, A., Chevallier, L., & Goosmann, R. W. 2006, *A&A*, 451, L23
- Grevesse, N., Noels, A., & Sauval, A. J. 1996, in *Astronomical Society of the Pacific Conference Series*, 117

- Huber, P. J. 1964. *Robust Estimation of a Location Parameter*. Annals of Mathematical Statistics 35:73-101.
- Kaastra, J. S., Mewe, R., Liedahl, D. A., Komossa, S., & Brinkman, A. C. 2000, A&A, 354, L83
- Kallman, T. & Bautista, M. 2001, ApJS, 133, 221
- Kallman, T. R. & McCray, R. 1982, ApJS, 50, 263
- Kaspi, S., Brandt, W. N., George, I. M., Netzer, H., Crenshaw, D. M., Gabel, J. R., Hamann, F. W., Kaiser, M. E., Koratkar, A., Kraemer, S. B., Kriss, G. A., Mathur, S., Mushotzky, R. F., Nandra, K., Peterson, B. M., Shields, J. C., Turner, T. J., & Zheng, W. 2002, ApJ, 574, 643
- Kaspi, S., Brandt, W. N., Netzer, H., George, I. M., Chartas, G., Behar, E., Sambruna, R. M., Garmire, G. P., & Nousek, J. A. 2001, ApJ, 554, 216
- Kaspi, S., Brandt, W. N., Netzer, H., Sambruna, R., Chartas, G., Garmire, G. P., & Nousek, J. A. 2000, ApJ, 535, L17
- Knigge, C., Woods, J. A., & Drew, J. E. 1995, MNRAS, 273, 225
- Komossa, S. 1999, ISAS Report, p. 149-160, T. Takahashi, H. Inoue (eds), 149
- Kraemer, S. B., Crenshaw, D. M., & Gabel, J. R. 2001, ApJ, 557, 30
- Krolik, J. H. & Kriss, G. A. 2001, ApJ, 561, 684
- Krongold, Y., Nicastro, F., Brickhouse, N. S., Elvis, M., Liedahl, D. A., & Mathur, S. 2003, ApJ, 597, 832
- Krongold, Y., Nicastro, F., Elvis, M., Brickhouse, N. S., Mathur, S., & Zezas, A. 2005, ApJ, 620, 165
- Lamers, H. J. G. L. M., Cerruti-Sola, M., & Perinotto, M. 1987, ApJ, 314, 726
- Murray, N., Chiang, J., Grossman, S. A., & Voit, G. M. 1995, ApJ, 451, 498
- Netzer, H., Kaspi, S., Behar, E., Brandt, W. N., Chelouche, D., George, I. M., Crenshaw, D. M., Gabel, J. R., Hamann, F. W., Kraemer, S. B., Kriss, G. A., Nandra, K., Peterson, B. M., Shields, J. C., & Turner, T. J. 2003, ApJ, 599, 933
- Ogle, P. M., Marshall, H. L., Lee, J. C., & Canizares, C. R. 2000, ApJ, 545, L81

- Peterson, B. M., Ferrarese, L., Gilbert, K. M., Kaspi, S., Malkan, M. A., Maoz, D., Merritt, D., Netzer, H., Onken, C. A., Pogge, R. W., Vestergaard, M., & Wandel, A. 2004, *ApJ*, 613, 682
- Proga, D. 2003, *ApJ*, 592, L9
- Proga, D., Stone, J. M., & Kallman, T. R. 2000, *ApJ*, 543, 686
- Ramírez, J. M. 2008, *A&A*, 489, 57
- Ramírez, J. M., Bautista, M., & Kallman, T. 2005, *ApJ*, 627, 166
- Reeves, J. N., Nandra, K., George, I. M., Pounds, K. A., Turner, T. J., & Yaqoob, T. 2004, *ApJ*, 602, 648
- Rózańska, A., Goosmann, R., Dumont, A., & Czerny, B. 2006, *A&A*, 452, 1
- Saez, C., Chartas, G., & Brandt, W. N. 2009, *ApJ*, 697, 194
- Shields, J. C. & Hamann, F. 1997, *ApJ*, 481, 752
- Shlosman, I., Vitello, P., & Mauche, C. W. 1996, *ApJ*, 461, 377
- Steenbrugge, K. C., Kaastra, J. S., de Vries, C. P., & Edelson, R. 2003, *A&A*, 402, 477
- Tarter, C. B., Tucker, W. H., & Salpeter, E. E. 1969, *ApJ*, 156, 943
- Yaqoob, T., McKernan, B., Kraemer, S. B., Crenshaw, D. M., Gabel, J. R., George, I. M., & Turner, T. J. 2003, *ApJ*, 582, 105

Table 1. Composition and parameter values of the kinematics model A. <sup>a</sup>

Element	Relative Abundance
H ...	1.0
He ...	0.1
C ...	0.3540E-03
N ...	0.9330E-04
O ...	0.7410E-03
Ne ...	0.1200E-03
Mg ...	0.3800E-04
Si ...	0.3550E-04
S ...	0.2140E-04
Ar ...	0.3310E-05
Ca ...	0.2290E-05
Fe ...	0.3160E-04

<sup>a</sup>In this model  $w_0 = 0.4$ ,  $v_\infty = 900 \text{ km s}^{-1}$ ,  $\log_{10} r_0 = 15.75 \text{ [cm]}$ ,  $v_{turb} = 200 \text{ km s}^{-1}$  and  $N_H = 5 \times 10^{20} \text{ cm}^{-2}$ .

Table 2. Composition and parameter values of the kinematics model B. <sup>a</sup>

Element	Relative Abundance
H ...	1.0
He ...	0.1
C ...	0.3540E-03
N ...	0.9330E-04
O ...	0.7410E-03
Ne ...	0.1200E-03
Mg ...	0.3800E-04
Si ...	0.3550E-04
S ...	0.2140E-04
Ar ...	0.3310E-05
Ca ...	0.2290E-05
Fe ...	0.3160E-04

<sup>a</sup>In this model  $w_0 = 0.4$ ,  $v_\infty = 1100 \text{ km s}^{-1}$ ,  $\log_{10} r_0 = 15.75 \text{ [cm]}$ ,  $v_{turb} = 200 \text{ km s}^{-1}$  and  $N_H = 5 \times 10^{20} \text{ cm}^{-2}$ .

Table 3. Asymmetry comparison between model A and observation

Ion	Line ( $\text{\AA}$ )	$v(\tau_{max})/900 \text{ km s}^{-1}$	Ramírez et al. (2005) <sup>a</sup>
S xvi	4.729	0.55 (R)	$0.33 \pm 0.1$ (B)
S xv	5.039	0.67 (R)	$0.23 \pm 0.1$ (B)
Si xiii	5.681	0.70 (R)	$0.35 \pm 0.1$ (B)
Si xiv	6.182	0.67 (R)	$0.23 \pm 0.08$ (B)
Si xiii	6.648	0.70 (R)	$0.43 \pm 0.074$ (B)
Mg xii	7.106	0.70 (R)	$0.32 \pm 0.070$ (B)
Mg xi	7.473	0.76 (R)	$0.74 \pm 0.067$ (R)
Fe xxiii	8.303	0.55 (R)	$0.037 \pm 0.060$ (B)
Mg xii	8.421	0.70 (R)	$0.32 \pm 0.059$ (B)
Mg xi	9.169	0.76 (R)	$0.31 \pm 0.054$ (B)
Ne x	9.708	0.76 (R)	$0.45 \pm 0.052$ (B)
Ne x	10.240	0.76 (R)	$0.17 \pm 0.048$ (B)
Ne ix	11.547	0.82 (R)	$0.69 \pm 0.043$ (R)
Fe xxii	11.770	0.55 (R)	$0.22 \pm 0.042$ (B)
Ne x	12.134	0.76 (R)	$0.29 \pm 0.041$ (B)
Fe xxi	12.284	0.62 (R)	$0.42 \pm 0.040$ (B)
Fe xviii	14.373	0.70 (R)	$0.27 \pm 0.035$ (B)
Fe xviii	14.534	0.70 (R)	$0.51 \pm 0.034$ (R)
O viii	14.832	0.82 (R)	$0.21 \pm 0.033$ (B)
Fe xvii	15.015	0.70 (R)	$0.76 \pm 0.033$ (R)
O viii	15.188	0.82 (R)	$0.38 \pm 0.033$ (B)
O viii	16.006	0.82 (R)	$0.26 \pm 0.030$ (B)
O vii	17.200	0.90 (R)	$0.29 \pm 0.029$ (B)
O vii	17.396	0.90 (R)	$0.30 \pm 0.029$ (B)
O vii	17.768	0.90 (R)	$0.32 \pm 0.028$ (B)
O vii	18.627	0.90 (R)	$0.32 \pm 0.027$ (B)
O viii	18.969	0.82 (R)	$0.26 \pm 0.026$ (B)

<sup>a</sup> $\bar{v}/v_1$ , see definition in the text.

Table 4. Parameters of the two outflows model (Model C)

Outflow HIF	Outflow LIF
$\log \xi_0 = 3.0$	$\log \xi_0 = 2.0$
$v_\infty = 1100 \text{ km s}^{-1}$	$v_\infty = 2200 \text{ km s}^{-1}$
$N_H = 10^{22} \text{ cm}^{-2}$	$N_H = 10^{21} \text{ cm}^{-2}$
$w_0 = 0.4$	$w_0 = 0.2$
Solar composition	Solar composition

Table 5. Asymmetry comparison between model C and observation

Ion	Line ( $\text{\AA}$ )	$v(\tau_{max}[\text{HIF}])/1100 \text{ km s}^{-1}$	$v(\tau_{max}[\text{HIF}+\text{LIF}])/2200 \text{ km s}^{-1}$
S xvi	4.729	0.47 (B)	0.47 (B)
S xv	5.039	0.55 (R)	0.55 (R)
Si xiii	5.681	0.62 (R)	0.62 (R)
Si xiv	6.182	0.55 (R)	0.55 (R)
Si xiii	6.648	0.62 (R)	0.62 (R)
Mg xii	7.106	0.55 (R)	0.55 (R)
Mg xi	7.473	0.74 (R)	0.74 (R)
Fe xxiii	8.303	0.47 (B)	0.47 (B)
Mg xii	8.421	0.55 (R)	0.55 (R)
Mg xi	9.169	0.74 (R)	0.37 (B) <sup>a</sup>
Ne x	9.708	0.74 (R)	0.74 (R)
Ne x	10.240	0.74 (R)	0.37 (B) <sup>a</sup>
Ne ix	11.547	0.74 (R)	0.37 (B) <sup>a</sup>
Fe xxii	11.770	0.47 (B)	0.47 (B)
Ne x	12.134	0.74 (R)	0.37 (B) <sup>a</sup>
Fe xxi	12.284	0.47 (B)	0.47 (B)
Fe xviii	14.373	0.55 (R)	0.55 (R)
Fe xviii	14.534	0.55 (R)	0.55 (R)
O viii	14.832	0.74 (R)	0.37 (B) <sup>a</sup>
Fe xvii	15.015	0.62 (R)	0.62 (R)
O viii	15.188	0.74 (R)	0.37 (B) <sup>a</sup>
O viii	16.006	0.74 (R)	0.37 (B) <sup>a</sup>
O vii	17.200	0.82 (R)	0.41 (B) <sup>a</sup>
O vii	17.396	0.82 (R)	0.41 (B) <sup>a</sup>
O vii	17.768	0.82 (R)	0.41 (B) <sup>a</sup>
O vii	18.627	0.82 (R)	0.41 (B) <sup>a</sup>
O viii	18.969	0.74 (R)	0.37 (B) <sup>a</sup>

<sup>a</sup>With the addition of the LIF, we mark those line whose symmetry change.



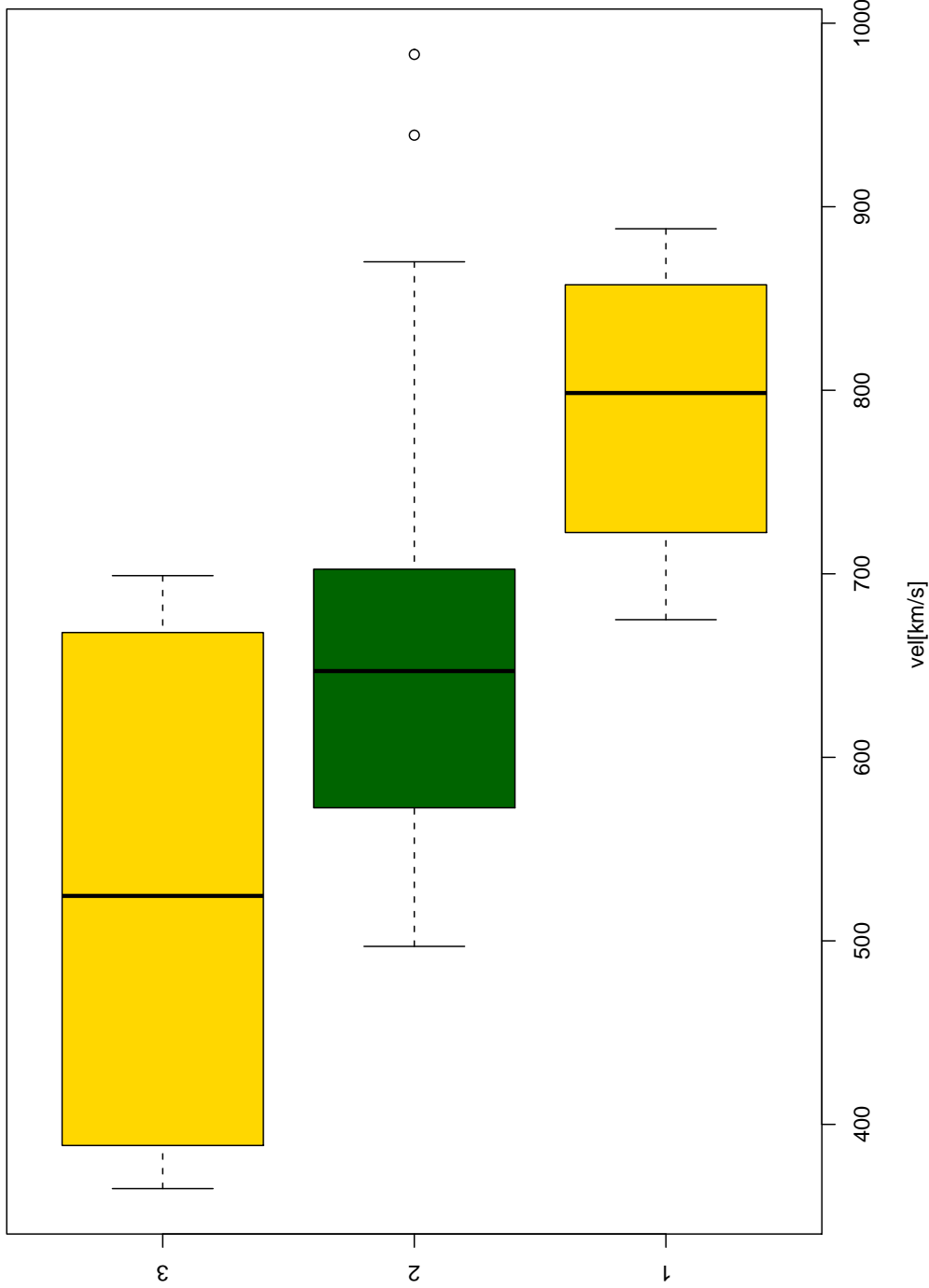


Fig. 1.— Statistical significance of the shifting of the X-ray lines found in the spectrum of NGC 3783. Each box is made of five-number summaries: the smallest observation (sample minimum, which are the extreme thin bars at the left of each box), a lower quartile (Q1, which is the left thick border of each box), median (Q2, black thick vertical line), upper quartile (Q3, the right thick border of each box) and largest observation (sample maximum, which are the extreme thin bars at the right of each box).

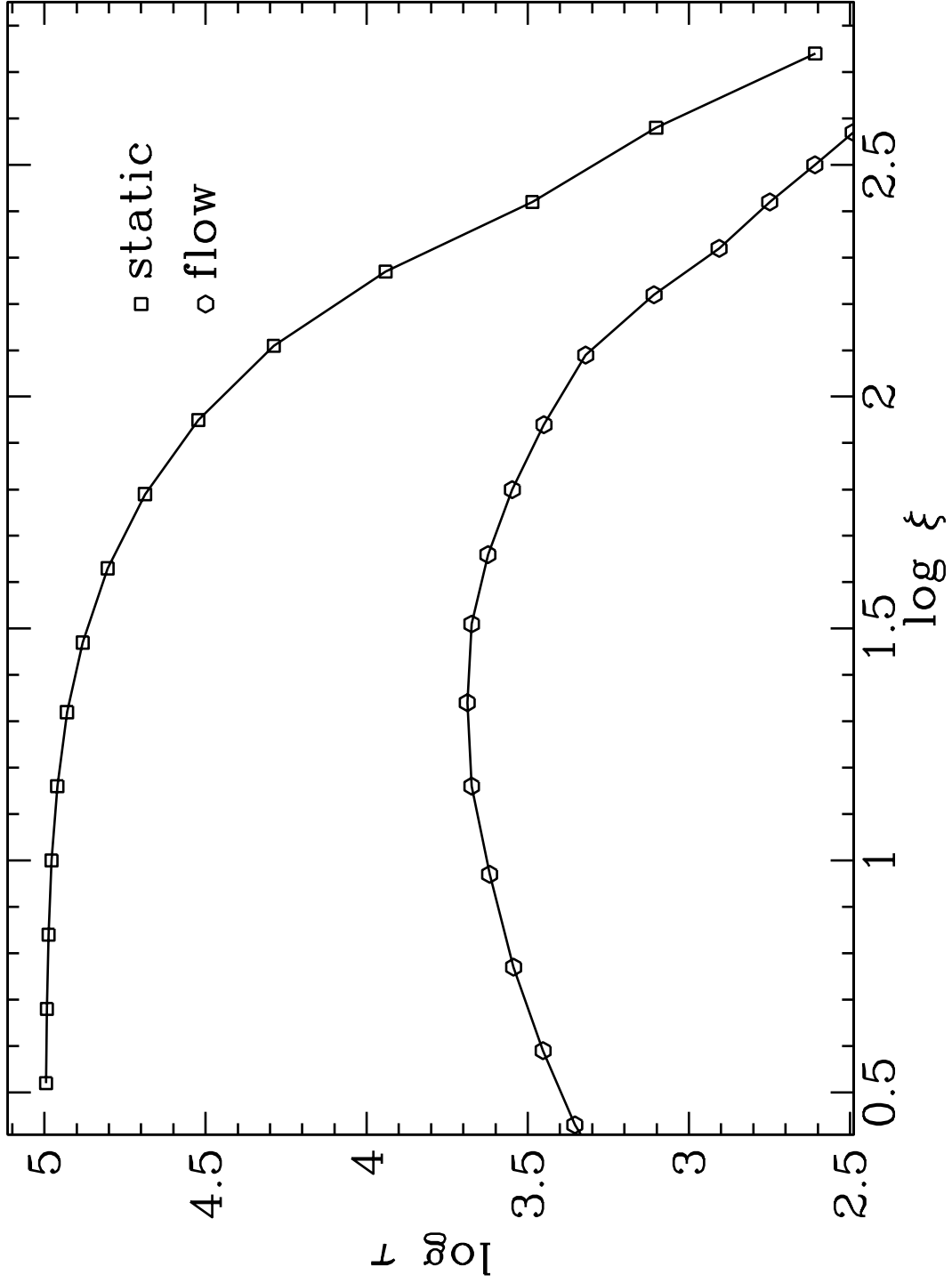


Fig. 2.— Optical depth ( $\tau$ ) static case *vs* outflow model for the line Ne x  $\lambda 12.134$  (see text).

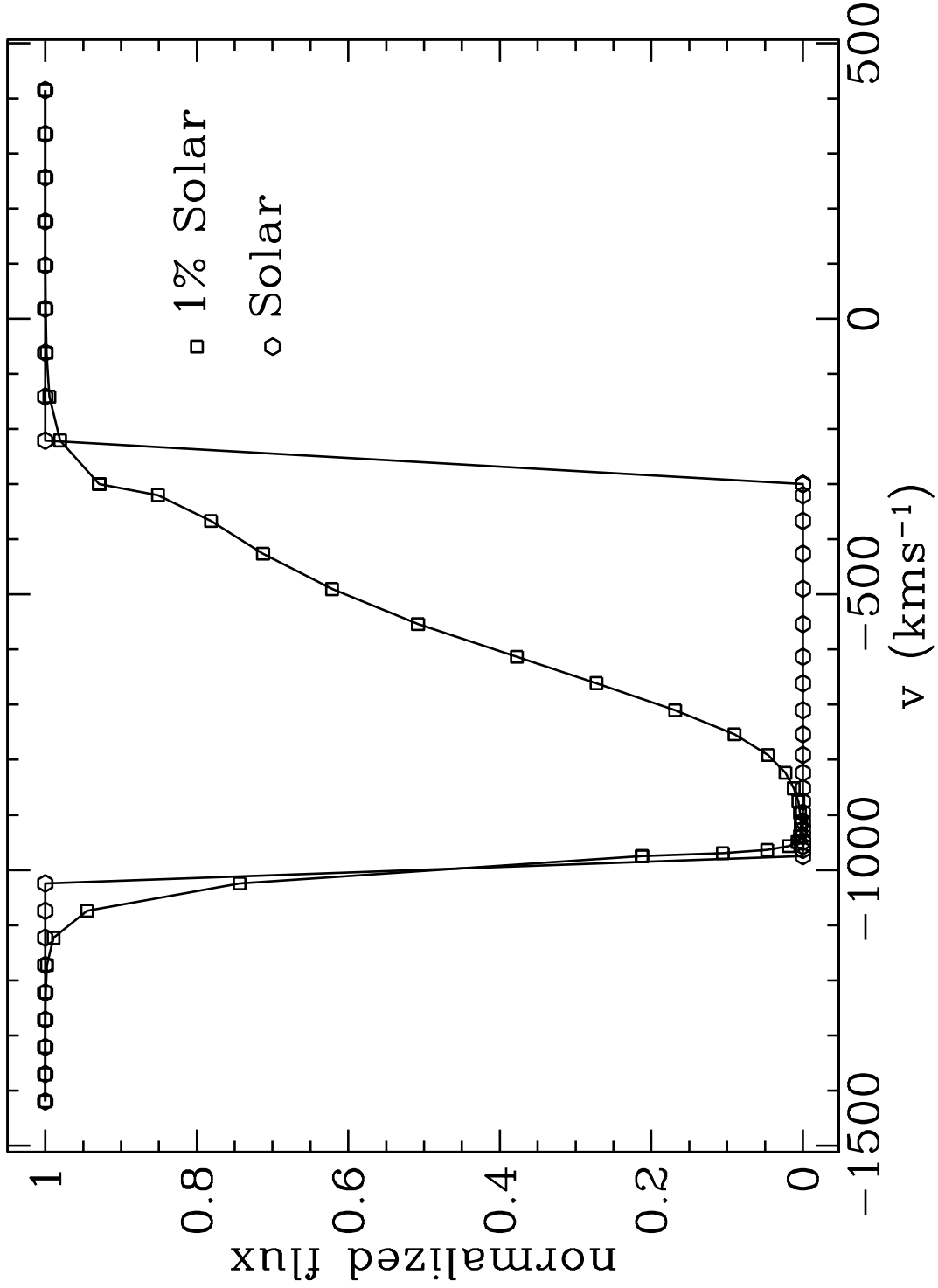


Fig. 3.— Profile of the line Ne x  $\lambda 12.134$  formed by taking  $F_{\lambda}(v) = F_c \times \exp[-\tau_{\lambda}(v)]$  as function of the velocity. The rectangle profile is made by a cloud with solar abundances (open circles). The profile with an extended red wing and a sharp blue wing is made by a cloud with 1% solar abundances (open square).

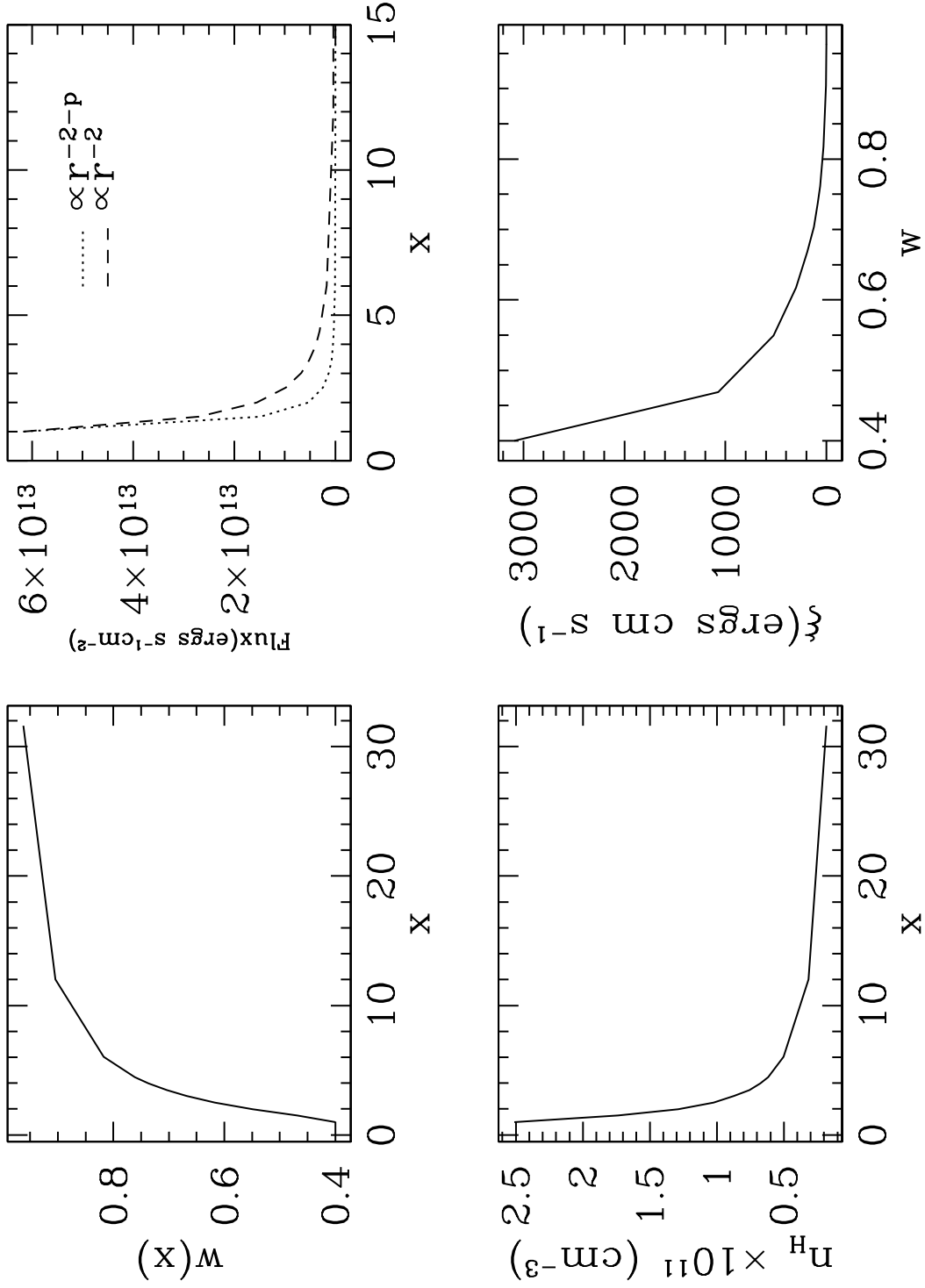


Fig. 4.— Variation of the main kinematic and ionization variables for model A (see text). *Upper left:* Velocity law  $w(x)$  for the model. *Upper right:* The ionizing radiative flux, decaying with  $\propto r^{-2}$  (dashed line) and with  $\propto r^{-2-p}$  (dotted line). *Lower left:* Variation of the density as function of  $x$ . *Lower right:* Variation of the ionization parameter ( $\xi$ ) with the normalized velocity.

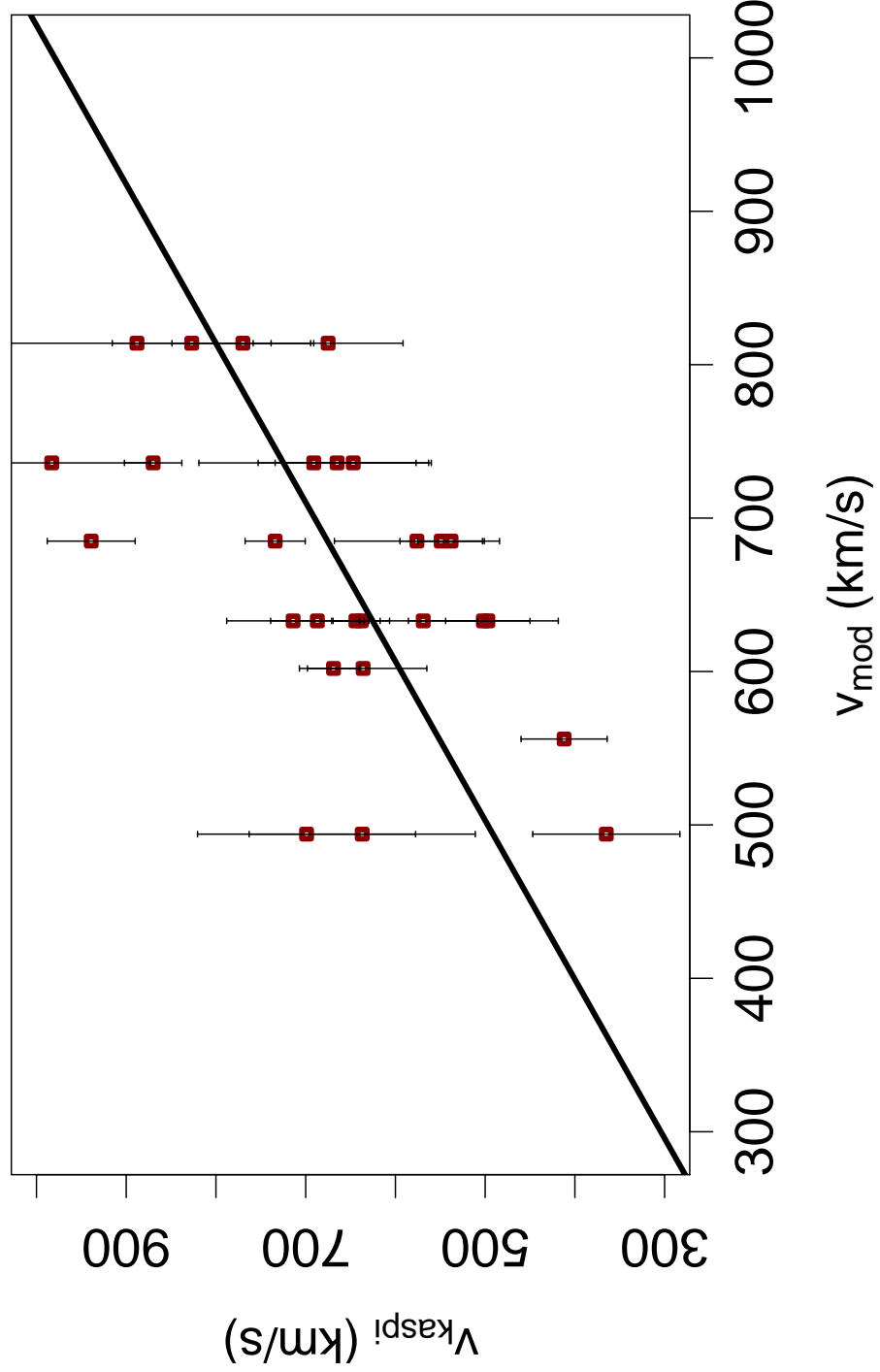


Fig. 5.— Measured  $v$ s model predicted velocities for the group of unblended lines given in Table 2 of Ramírez et al. (2005). The measurements are taken from Kaspi et al. (2002). The solid line is the best line after a linear regression for model A.

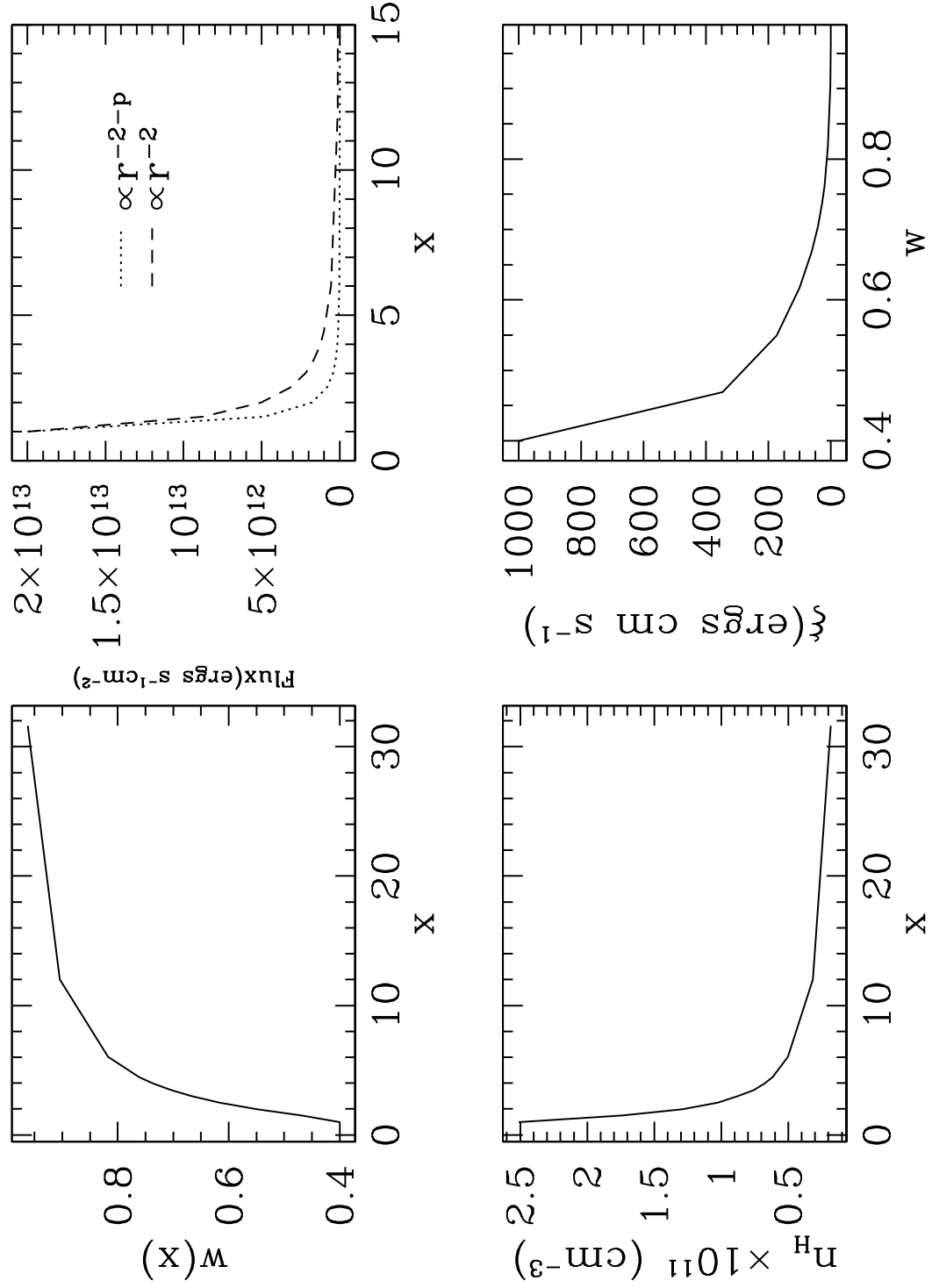


Fig. 6.— Variation of the main kinematic and ionization variables for model B (see text). *Upper left:* Velocity law  $w(x)$  for the model. *Upper right:* The ionizing radiative flux, decaying with  $\propto r^{-2}$  (dashed line) and with  $\propto r^{-2-p}$  (dotted line). *Lower left:* Variation of the density as function of  $x$ . *Lower right:* Variation of the ionization parameter ( $\xi$ ) with the normalized velocity.

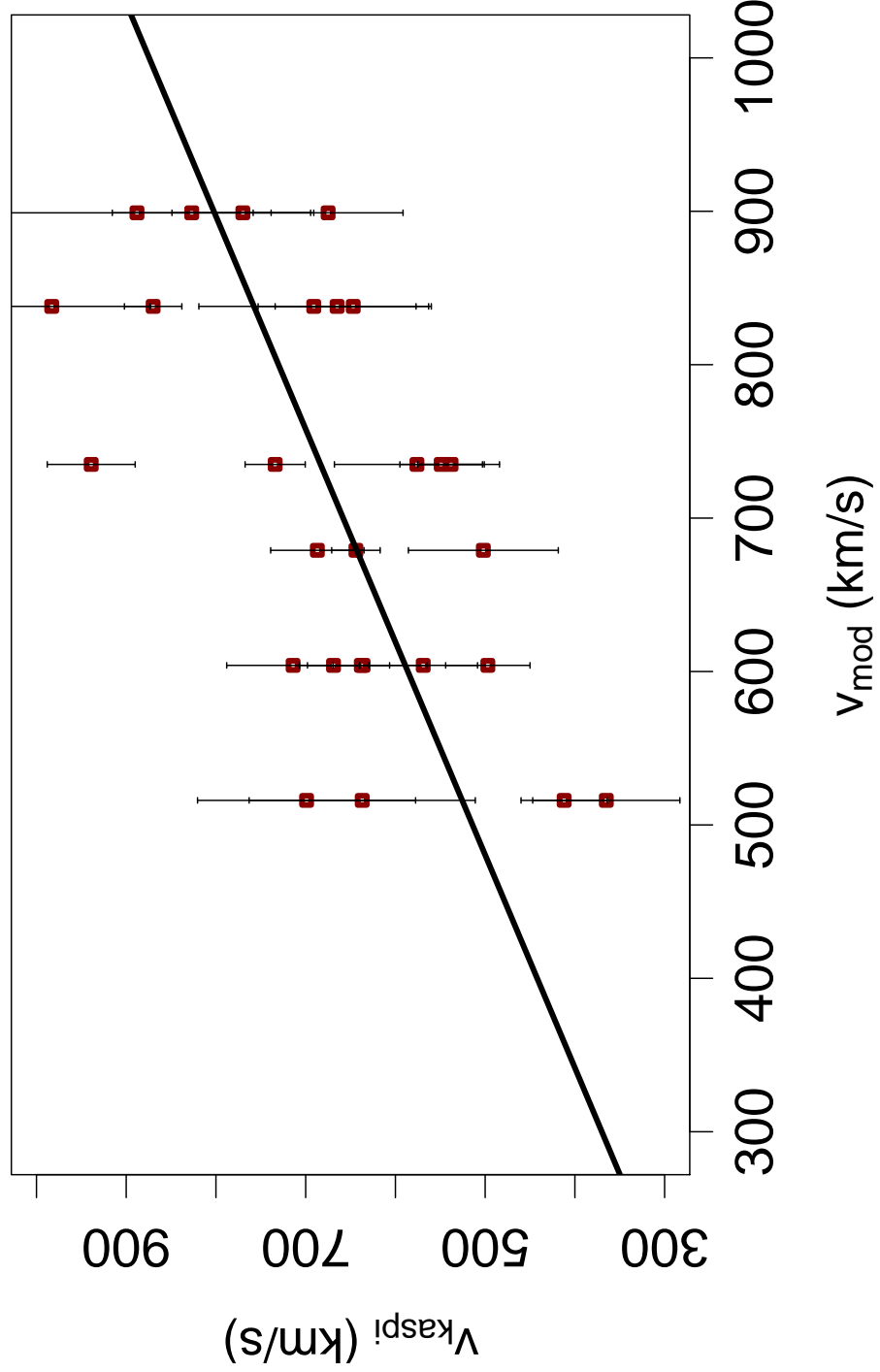


Fig. 7.— Measured  $vs$  model predicted velocities for the group of unblended lines given in Table 2 of Ramírez et al. (2005). The measurements are taken from Kaspi et al. (2002). The solid line is the best line after a linear regression for model B.

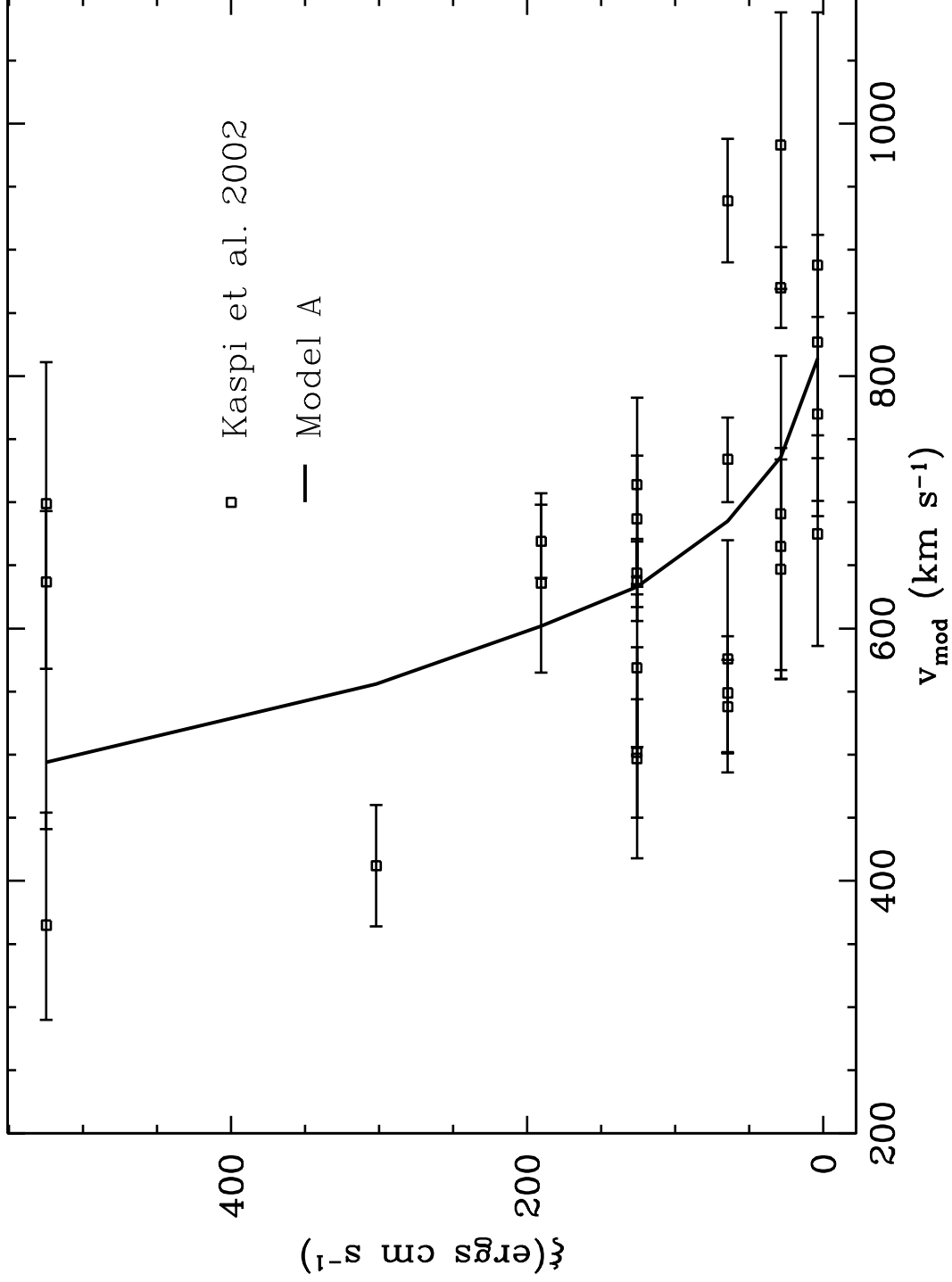


Fig. 8.— Relationship between the ionization parameter and velocity. The solid line is the theoretical prediction for model A. The open squares with error bars are points with velocities taken from Kaspi et al. (2002), for the group of lines compared in Figure 5.



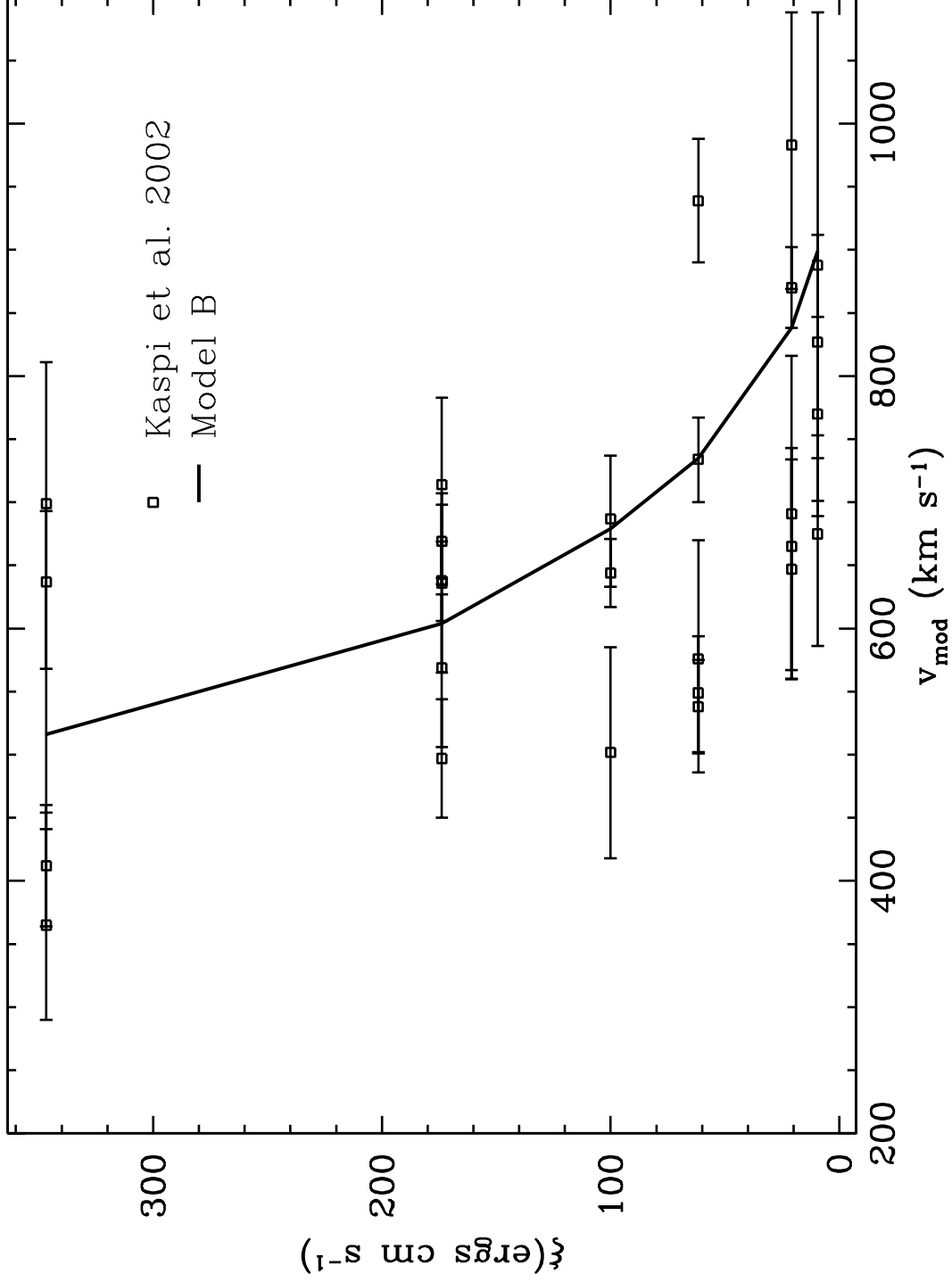


Fig. 9.— Relationship between the ionization parameter and velocity. The solid line is the theoretical prediction for model B. The open squares with error bars are points with velocities taken from Kaspi et al. (2002), for the group of lines compared in Figure 7.

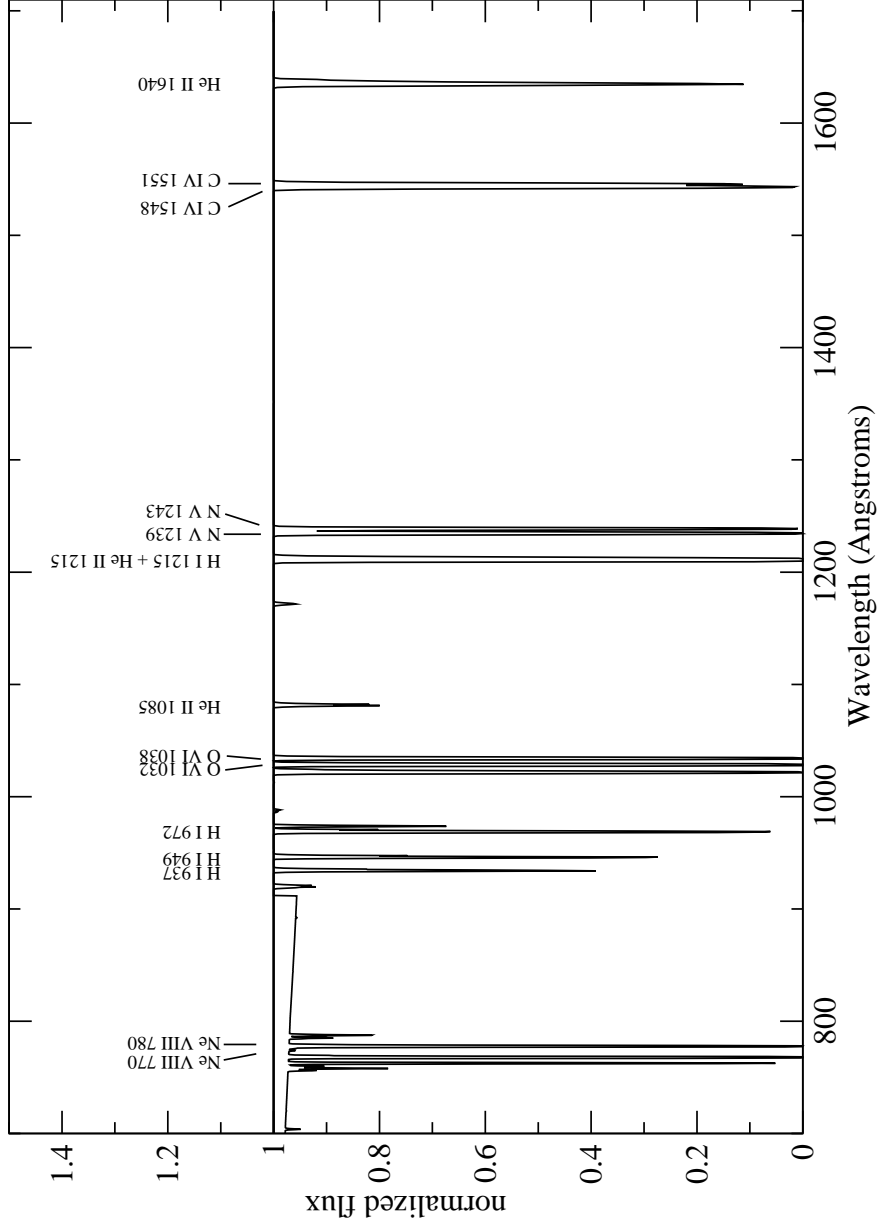


Fig. 10.— Predicted UV spectrum by model B (in the range 700-1700 Å). These absorption lines are formed by the faster (or at lower ionization parameters) clouds of model B, i.e.,  $\log \xi = 0.12, -0.65$ . Most of these lines are found in real UV spectrum of AGN.

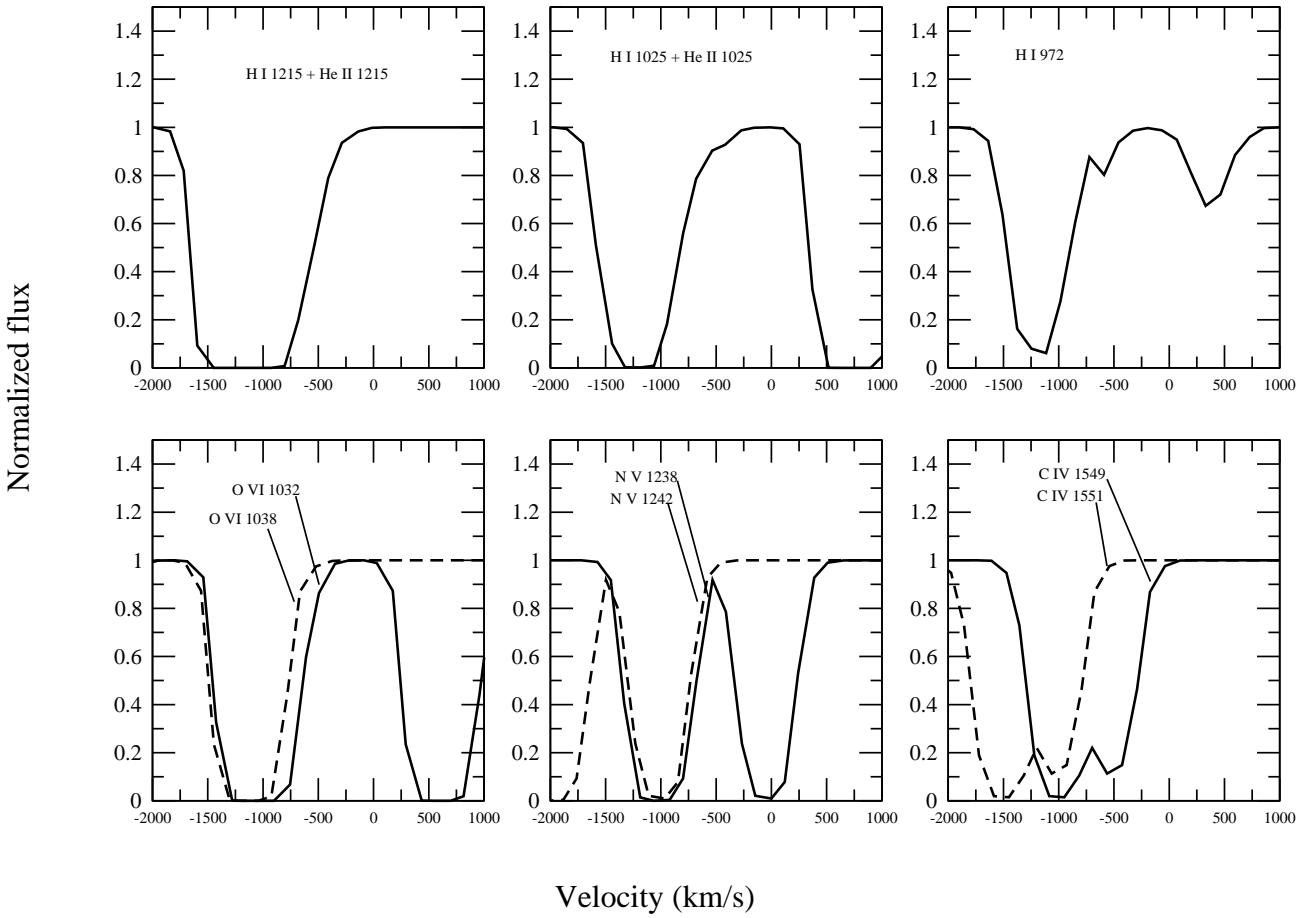


Fig. 11.— Predicted UV spectrum by model B (in the velocity space). These absorption lines are formed by the faster (or at lower ionization parameters) clouds of model B, i.e.,  $\log \xi = 0.12, -0.65$ . Some of the velocities displayed by these lines are shared by lines coming from the X-ray band. For transforming to velocity space, we have taken the shorter rest-wavelength of the doublet (solid line), and also the longer rest-wavelength of the doublet (dashed line).

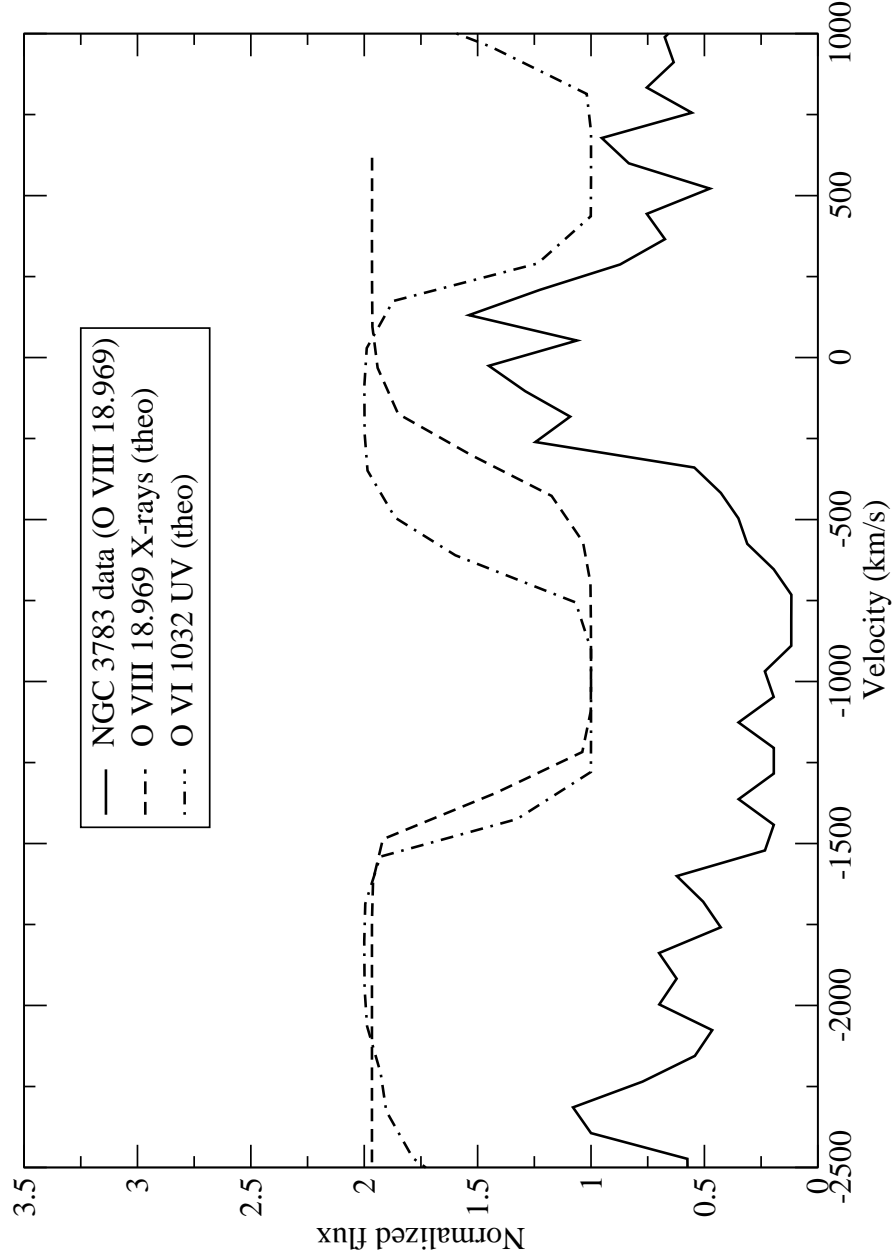


Fig. 12.— Possible kinematical relationship between the UV and the X-ray absorbers. In the figure are plotted the theoretical X-ray and UV lines O VIII  $\lambda 18.969$  and O VI  $\lambda 1032$ , dashed and short-dotted lines respectively. Also plotted the profile of the line O VIII  $\lambda 18.969$  taken from the 900 ks spectrum of NGC 3783. All these lines are sharing velocities  $\sim 1000$  km s $^{-1}$ .

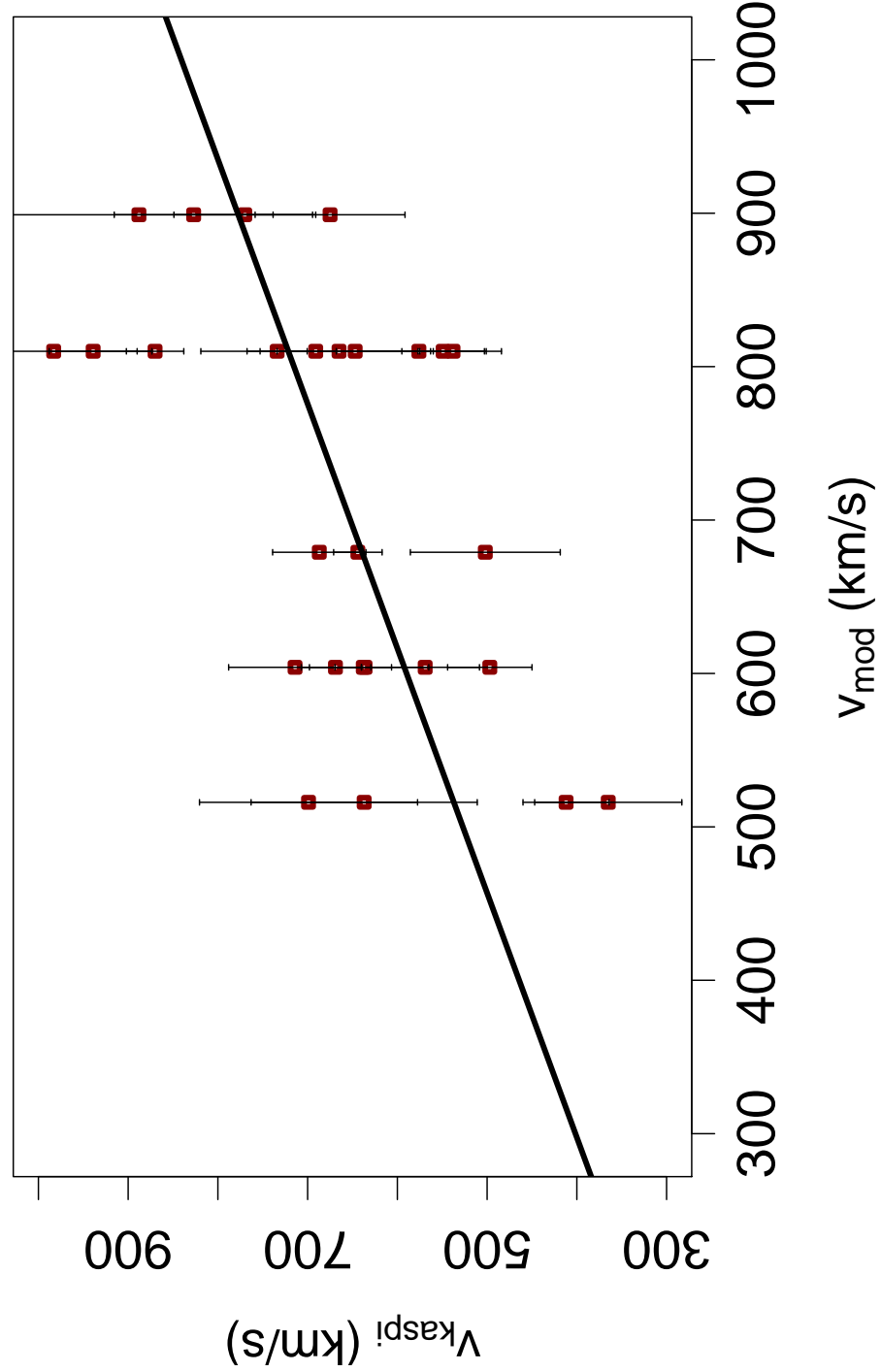


Fig. 13.— Measured *vs* model predicted velocities for the group of unblended lines given in Table 2 of Ramírez et al. (2005). The measurements are taken from Kaspi et al. (2002). The solid line is the best line after a linear regression for model C.

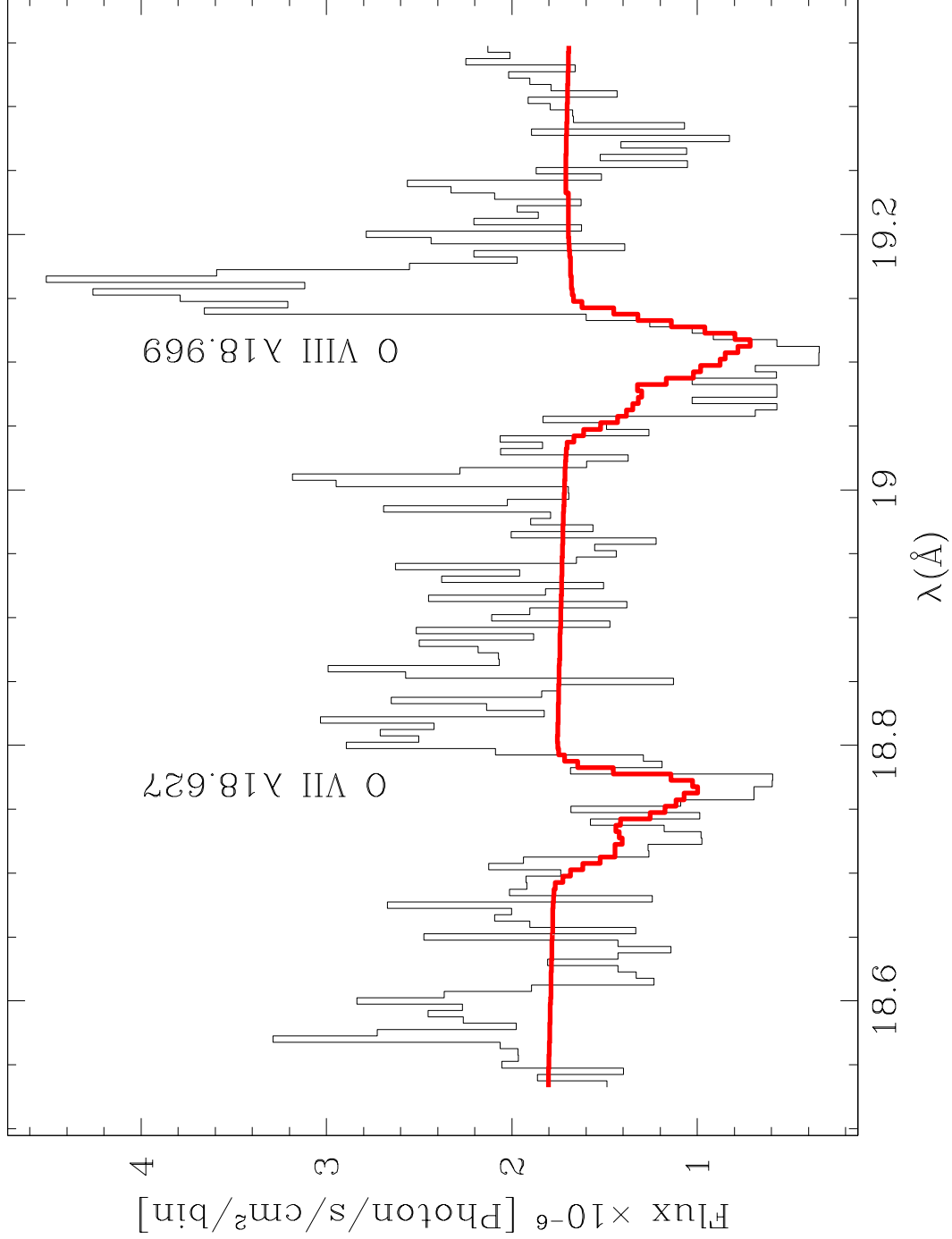


Fig. 14.— A graphical representation of the flows HIF and LIF with the line profiles seen in NGC 3783 (histogram). Solid line is the composed model (model C) by the two flows. It can be seen that it was necessary to include the second low ionization flow in order to reproduce the asymmetry of these lines. Otherwise the high ionization flow would form a more extended red wing.